Magnetic Resonance Imaging 61 (2019) 207–223

Contents lists available at ScienceDirect

Magnetic Resonance Imaging

journal homepage: www.elsevier.com/locate/mri

Original contribution

# Retrospective correction of intensity inhomogeneity with sparsity constraints in transform-domain: Application to brain MRI

Maryjo M. George, Kalaivani S.*

*School of Electronics Engineering, Vellore Institute of Technology, Vellore, Tamil Nadu 632014, India*

ARTICLE INFO

*Keywords:*
Intensity inhomogeneity correction
Bias field
MRI
Sparsity constraints
$L_1$ norm minimization

ABSTRACT

An effective retrospective correction method is introduced in this paper for intensity inhomogeneity which is an inherent artifact in MR images. Intensity inhomogeneity problem is formulated as the decomposition of acquired image into true image and bias field which are expected to have sparse approximation in suitable transform domains based on their known properties. Piecewise constant nature of the true image lends itself to have a sparse approximation in framelet domain. While spatially smooth property of the bias field supports a sparse representation in Fourier domain. The algorithm attains optimal results by seeking the sparsest solutions for the unknown variables in the search space through $L_1$ norm minimization. The objective function associated with defined problem is convex and is efficiently solved by the linearized alternating direction method. Thus, the method estimates the optimal true image and bias field simultaneously in an $L_1$ norm minimization framework by promoting sparsity of the solutions in suitable transform domains. Furthermore, the methodology doesn't require any preprocessing, any predefined specifications or parametric models that are critically controlled by user-defined parameters. The qualitative and quantitative validation of the proposed methodology in simulated and real human brain MR images demonstrates the efficacy and superiority in performance compared to some of the distinguished algorithms for intensity inhomogeneity correction.

## 1. Introduction

Magnetic Resonance Imaging (MRI) and its variants are extensively employed for human brain analysis as they deliver high resolution images non-invasively. However, the inherent artifacts present in raw MR images may have a substantial impact on numerous commonly used automatic medical image processing techniques in clinical applications such as segmentation and registration [1–3]. One among the potential artifacts is the intensity inhomogeneity as it alters the intensity levels of homogenous tissue regions with respect to location. Moreover, this artifact is severe in high strength field MRI scanners and can even restrict visual analysis of MR images [4].

Intensity inhomogeneity artifact also known as bias field, occurs from two sources: the hardware and the subject [5–8]. Intensity inhomogeneity from the hardware is caused by static magnetic field heterogeneity, reception coil heterogeneous sensitivity and eddy currents from gradient coils. The subject introduced inhomogeneity depends on the dielectric properties, magnetic permeability and orientation of the subject inside the scanner. Andrzej Materka and Michal Strzelecki have clearly demonstrated the importance of intensity inhomogeneity correction prior to the texture analysis based MR image quantification [9]. The bias field correction strategies existing in the literature can be broadly categorized into retrospective and prospective corrections [10]. The prospective corrections focus on the calibration of the MRI acquisition process and are therefore ineffective to correct inhomogeneity introduced by the subject. Whereas, the source of inhomogeneity is inconsequential to the accuracy of retrospective techniques as they rely solely on information from the acquired images.

According to the literature survey of Vovk et al. [10], the retrospective correction techniques can be classified into filtering-, segmentation-, histogram- and surface fitting- based strategies. The retrospective methods exploit the fact that the bias field is a spatially smooth multiplicative artifact. Filtering methods utilize a low-pass filter mainly, mean [11] or median filter [12] to extract the smoothly varying bias field. Some of the advanced filtering techniques in the literature extract the bias field through spatial-frequency decomposition of the acquired image [13]. However, the optimal parameter selection of the filters is a deciding factor in the accuracy of the filtering based approaches. Further, the segmentation based methods yield simultaneous segmentation and correction as the estimation of the bias field is guided through a segmentation process. And the preferable techniques for segmentation are maximum likelihood or maximum a posteriori

* Corresponding author.
*E-mail addresses:* maryjom.george2015@vit.ac.in (M.M. George), kalaivani.s@vit.ac.in (S. Kalaivani).

https://doi.org/10.1016/j.mri.2019.04.011
Received 20 December 2018; Received in revised form 5 April 2019; Accepted 18 April 2019

probability (MAP) [14–16], fuzzy c-means (FCM) [17–19] and non-parametric clustering such as meanshift and maxshift [20,21]. The mathematical image model was modified in the aforementioned standard segmentations to incorporate the multiplicative effect of the artifact to extract an accurate segmentation thereby facilitating simultaneous bias field estimation. A new multiplicative intrinsic component optimization (MICO) has been presented by Li et al. [22] where bias field smoothness is ensured by linear combination of 20 polynomial basis functions. The convergence of the method is independent of initialization and is relatively fast. However, the segmentation is based on fuzzy clustering and does not consider spatial information for the clustering. The state-of-art method, N4 [23] is a histogram based technique that seeks a slowly varying bias field that maximizes the high frequency histogram contents. Many of the surface fitting methods approximate the bias field to a slowly varying parametric surface from significant points obtained after feature extraction in the acquired image through an iterative process [24–26]. The feature points are identified based on intensity or the gradients of intensities. Therefore, a typical constraint of the method is the existence of large homogeneous tissue region in the image. Albeit, certain segmentation based methods involved manual interaction and atlases for parameter initialization for instance, the tissue class model parameters.

The recent contributions to retrospective correction include approaches based on level set models that have gained widespread attention in medical image segmentation over the past decade as they facilitate easy representation and modification of complex topologies. Some of the level set methods interweave bias field estimation, segmentation and registration [27,28]. Li et al. [29] have proposed a region based variational level set framework to implement a local intensity clustering property that simultaneously obtains segmentation and bias field estimation. The proposed energy functional was not convex and could be trapped in local minima [30]. Zhan et al. [31] have introduced a method by improving the clustering in [29] with Gaussian distributions subjected to bias field as local region descriptor which enables identification of regions with identical mean intensities and different variances. The method was later modified in the works of Zhang et al. [30] where a more robust model was implemented and the maximum likelihood energy function was defined in a transformed domain. The mapping to the transformed domain enabled robustness to noise and better separation of intensity distributions. Ji et al. [32] have proposed a local likelihood image fitting variational approach based on the assumption that neighborhood are disjoint regions and the neighborhood statistics are utilized to construct the local likelihood function. Lately, Tang et al. [33] formulated a non-convex weighted energy integral which is a local Gaussian distribution fitting function with weights as local entropy. The local entropy estimated from local grey level histogram and is responsible for bias field correction and noise removal. However, this two-phase method has to be extended to multiphase level set formulation to enable brain MR segmentation. A Modified Mumford-Shah model [34] has been proposed by Yupping et al. in [35] where $L_0$ gradient regularizer is used for piecewise smooth approximation. The data fidelity term in the proposed model enables estimated field to be influenced by neighborhood and in addition $L_2$ norm of the gradients is penalized to achieve smooth bias field.

Recently, split Bregman method has been effectively utilized to solve the energy functional associated with level set methods [36,37]. Cui et al. [37] have developed a localized kernel mapping method for segmentation under intensity inhomogeneity by integrating the kernel mapping functions [38,39] formulated in local neighborhoods. The intensity inhomogeneity is ignored in the segmentation as the kernel mappings are defined in local regions. The energy function is solved via split Bregman method. But, the number of predefined parameters in the algorithm is high and also the kernel width and neighborhood radius are critical in the algorithm performance. Chen et al. [36] have presented a multi-phase level set method where a local energy function depict local Gaussian distributions in a neighborhood using a kernel function. The local energy functions integrated over the image domain is optimized using split Bregman method. Ivanovska et al. [40] introduced a two-phase segmentation method where energy function included intensity clustering property proposed by Li et al. [29] and an explicit TV regularization for bias field. Yang et al. have proposed models for simultaneous bias field estimation and segmentation applying split Bregman method such as region scalable fitting [41], multiphase Vese-Chan model [42] and an enhanced local and global intensity fitting model [43,44]. Lately, Yang et al. [45] have presented an enhanced two-phase level set evolution model with split Bregman method with extension to multi-phase and the vector valued formulations. Inspired from the MICO model [22], Meng et al. [46] have developed an active contour method that utilizes a linear combination of orthogonal basis functions to improve the smoothness of the estimated bias field. Also, the method implements Student's t-distribution fitting to image intensity and hidden markov model to incorporate spatial information to improve the robustness to noise and weak edges. The energy function constructed is convex and was optimized through split Bregman algorithm.

It is to be remarked that many of the aforementioned works on intensity inhomogeneity correction adopt a predefined parametric model to the spatially slowly varying bias field. This strategy for bias field estimation is shown to be robust against noise as well. However, there are several shortcomings to the parametric model approximation. The parameters of the model need to be predefined and are significant in controlling the smoothness of the estimated bias field thereby critical in deciding the accuracy of correction [47]. In Bspline based fitting [48–50], the distance between the knots is to be user specified. And in multivariate polynomial based model fitting [26,51], the degree of bias field smoothness is conditioned on the order of the polynomial which is user-defined. Accordingly, in many of the model fitting methods, degree of smoothness of the bias field cannot be specified adaptively rather needs to be predefined. Apart from the parametric model fitting for bias field, the segmentation based methods that utilize a probabilistic framework for correction also require predefined distribution parameters [14,17,52]. Consequently, the accuracy of the correction methods based on probability distributions such as the EM strategies greatly depends on the initializations made such as the class distribution parameters. The local region methods in the segmentation based correction strategies are sensitive to predefined window radius and are computationally intensive as they operate in local level. In general, the methods with too many parameters reduce robustness of the algorithm as they require a large number of tuning parameters which will ultimately result in numerical instability [35]. The current paper introduces an algorithm for intensity inhomogeneity correction that doesn't necessitate any predefined parameters that control the degree of smoothness of the bias field. The algorithm is an $L_1$ norm minimization framework that estimates bias field and true image effectively by promoting their sparsity in suitable transform domains.

The researches on sparse representations have received a lot of attention in the recent years and the same are shown to be effective in the image processing field for image denoising [53,54], inpainting [55–58] and reconstruction problems [59–61]. The sparsity constraints are suitable in solving the intensity inhomogeneity problem as the nature of bias field and true image supports sparse representations in a suitable transform domain. The true image is assumed to follow piecewise constant property as the intensities of different tissues regions are distinct and clear tissue region boundaries exist under the absence of intensity inhomogeneity. This spatial property favors sparse representation of the true image under a tight framelet system. Similarly, the spatially smooth property of bias field enables it to have a sparse representation in the Fourier domain corresponding to a low-frequency dominant spectrum which has been already demonstrated in the filtering based techniques for inhomogeneity correction. Besides, the proposed method estimates bias field based on the identical logic of filtering techniques without requiring any critical predefined

parameters such as the filter specifications. The intensity inhomogeneity correction is formulated as a decomposition problem of the acquired image into two sparse images in suitable transform domains. The sparse solutions are obtained by minimizing $L_1$ norm of the transformed coefficients. Further, the algorithm utilizes the linearized alternating direction method to efficiently solve the associated objective function that is convex and non-differential due to presence of $L_1$ norm.

The contents of this paper are organized as follows; the methodology section explains the image model and the formulation of the proposed $L_1$ norm minimization framework from a primitive energy minimization model. The results section demonstrates the validation of the proposed algorithm in both simulated and real human brain datasets. The subsequent section draws discussions and conclusions based on the findings in the result section. A brief introduction to the framelet transform is provided in the appendix.

## 2. Methodology

Intensity inhomogeneity is introduced in the images through a slowly varying multiplicative bias field. A stable mathematical model of the image degraded by intensity inhomogeneity and noise [62] is described as follows;

$$R(x,y) = S(x,y)B(x,y) + \eta \tag{1}$$

where $R(x,y)$ and $S(x,y)$ are the observed intensity and actual intensity levels at the location $(x,y)$. $\eta$ represents the additive noise present in the acquired image. The bias field at the location $(x,y)$ is denoted as $B(x,y)$ and the multiplicative effect of bias field becomes additive in log domain as given below.

$$r(x,y) = s(x,y) + b(x,y) + \eta_l \tag{2}$$

where, $r(x,y)$, $s(x,y)$ and $b(x,y)$ represent the log-transformed values of $R(x,y)$, $S(x,y)$ and $B(x,y)$ respectively. The noise term remains as a high frequency component in the log domain and is denoted as $\eta_l$.

### 2.1. The primitive energy minimization problem

The objective of any retrospective correction strategy is to accurately estimate the true image, $s$ when the acquired image, $r$ is known. The estimation of $s$ and $b$ simultaneously for a given $r$ from Eq. (2) using least squares $L^2$ fit as shown below is an ill-posed problem since two unknowns have to be solved from a single equation.

$$\arg\min_{s,b} \frac{1}{2}\|r - s - b\|_2^2 \tag{3}$$

This section details the evolution of the proposed $L_1$ norm minimization framework from a primitive energy minimization model built on the above ill-posed problem. The primitive minimization formulation is grounded on the work proposed by Xi Chen et al. [63] for intensity inhomogeneity correction in MR images. The above problem leads to stable solutions if certain constraints are imposed on the unknown variables to confine their search space. The constraints are applied based on the spatial properties of true image and bias field. Since an ideal MR brain image contains tissue regions of nearly uniform intensity, the true image, $s$ is expected to be piecewise constant. In the view of this fact, the uniformity in the tissue region intensity levels of the corrected image has been attained by constraining the total variation (TV) norm of the corrected image. Total variation is essentially the $L_1$ norm of the gradients. Since the bias field is known to be smoothly varying in spatial domain, the constraint on the bias field, $b$ should enforce it to be spatially smooth. It is realized by the extensively used regularization technique of penalizing $L_2$ norm of gradients to achieve a smooth function. Finally, the primitive energy minimization problem is formulated to solve $s$ and $b$ simultaneously with two regularization constraints and is defined as follows;

$$\arg\min_{s,b} E(s,b) = \arg\min_{s,b} \|r - s - b\|_2^2 + \alpha\,\|\nabla b\|_2^2 + \beta\,\|\nabla s\|_1 \tag{4}$$

The energy minimization problem defined in Eq. (4) simultaneously achieves a piecewise constant corrected image and a spatially smooth bias field. The regularization parameters in the minimization problem, $\alpha$ and $\beta$ decide the tradeoff between regularity and good fit of the solutions. It is to be noted before solving for $b$ and $s$ that $E$ is a convex function with respect to $b$ for a given value of $s$ and vice versa. However, the function $E$ is not jointly convex with respect to $b$ and $s$. Therefore, the joint minimization problem is solved using an alternating minimization (AM) algorithm that iteratively solves the associated Euler-Lagrange equations of the problem with respect to $b$ and $s$. The Euler-Lagrange equation of the energy function $E$ with respect to $b$ is as follows;

$$0 = r - s - b - \alpha\left(\frac{\partial^2 b}{\partial x^2} + \frac{\partial^2 b}{\partial y^2}\right) \tag{5}$$

$$0 = r - s - b - \alpha\Delta b \tag{6}$$

where $\Delta$ represents the Laplacian operator. And the Euler-Lagrange equation of the energy function with respect to $s$ is as given below;

$$0 = r - s - b - \beta\left(\frac{\partial}{\partial x}\frac{s_x}{\sqrt{{s_x}^2 + {s_y}^2}} + \frac{\partial}{\partial y}\frac{s_y}{\sqrt{{s_x}^2 + {s_y}^2}}\right) \tag{7}$$

$$0 = r - s - b - \beta\nabla.\left(\frac{\nabla s}{|\nabla s|}\right) \tag{8}$$

The presence of the term $\frac{1}{|\nabla s|}$ makes Eq. (8) degenerate because of the singularity in the function when $s$ is locally constant. Therefore, a perturbation is added to the total variation norm and Eq. (8) is rewritten as

$$0 = r - s - b - \beta\nabla.\left(\frac{\nabla s}{\sqrt{|\nabla s|^2 + \varepsilon}}\right) \tag{9}$$

The images in the above formulation are interpreted as real valued functions defined on a domain, $\Omega$ that is bounded and open in $\mathbb{R}^2$. The above equations are formulated under homogeneous Neumann boundary condition ie. $\frac{\partial b}{\partial n} = 0$ and $\frac{\partial s}{\partial n} = 0$ on the boundary,$\partial\Omega$ respectively for Eqs. (6) and (9) where $n$ is the normal vector of $\partial\Omega$.

Let the known initial guess for $b$ and $s$ be $b^0$ and $s^0$. The AM scheme solves $E(s^0,b^1) \equiv \arg\min_b E(s^0,\bullet)$ followed by $E(s^1,b^1) \equiv \arg\min E(\bullet,b^0)$.Or equivalently, if $s^k$ and $b^k$ are known, $s^{k+1}$ and $b^{k+1}$are solved using AM as follows;

Solve for $b^{k+1}$from the following equation,

$$0 = r - s^k - b^{k+1} - \alpha\Delta b^{k+1} \tag{10}$$

Subsequently solve for $s^{k+1}$by solving,

$$0 = r - s^{n+1} - b^{n+1} - \beta\nabla.\left(\frac{\nabla s^{n+1}}{\sqrt{|\nabla s^{n+1}|^2 + \varepsilon}}\right) \tag{11}$$

In the AM scheme, the function $E$ always reduces with iterations. The equations Eq. (10) and Eq. (11) are solved using the basic time evolution approach introduced by Rudin et al. [64] where the solutions are considered as time dependent. More precisely, the optimal solution $b(x,y)$ is obtained when the steady state of the following parabolic equation is reached with a given initial condition;

$$\frac{\partial b}{\partial t} = r - s - b - \alpha\Delta b \;s.\,t.\; b(x,y,t)_{|t=0} = b^0 \tag{12}$$

Similarly, an optimal value for $s(x,y)$ is obtained as the solution of the parabolic equation given below,

$$\frac{\partial s}{\partial t} = r - s - b - \beta\nabla.\left(\frac{\nabla s}{\sqrt{|\nabla s|^2 + \varepsilon}}\right) s.\,t.\; s(x,y,t)_{|t=0} = s^0 \tag{13}$$

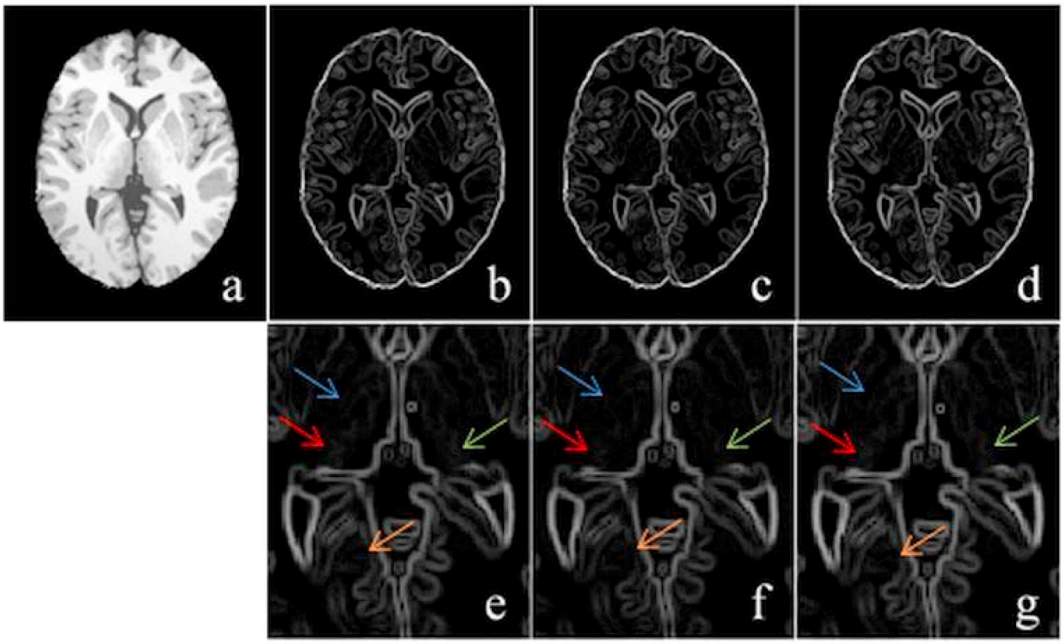


**Fig. 1.** Comparison of gradient maps of the corrected images. [a] Original T1-w axial simulated image (40% intensity inhomogeneity). Gradient maps of [b] 0% intensity inhomogeneity image [c] Corrected image from Algorithm 2.1 (using TV norm regularizer) [d] Corrected image from Algorithm 2.2 (using framelet norm regularizer), [e] Magnified portion of [b], [f] Magnified portion of [c], [g] Magnified portion of [d].

Here, the evolution in time is realized by considering a fixed time interval $\Delta t$. Subsequently, Eq. (12) is rewritten by considering the time step $\Delta t$ as follows;

$$\frac{b(t+\Delta t)-b(t)}{\Delta t} = r - s(t) - b(t) - \alpha \Delta b(t) \tag{14}$$

The optimal solution is obtained when $b$ converged to a steady state as $t$ increases. The numerical algorithm corresponding to the above equation as follows;

$$b_{ij}^{k+1} = b_{ij}^{k} + \frac{\Delta t}{h}\left[ r_{ij} - s_{ij}^{k} - b_{ij}^{k} - \alpha\left( \frac{b_{i+h,j}^{k} + b_{i-h,j}^{k} + b_{i,j+h}^{k} + b_{i,j-h}^{k} - 4b_{i,j}^{k}}{h^2} \right) \right] \tag{15}$$

Similarly, $s(t+\Delta t)$ is solved by rewriting Eq. (13) as follows;

$$\frac{s(t+\Delta t)-s(t)}{\Delta t} = r - s(t) - b(t+\Delta t) - \beta \nabla . \left( \frac{\nabla s(t)}{\sqrt{|\nabla s(t)|^2 + \varepsilon}} \right) \tag{16}$$

$$s_{ij}^{k+1} = s_{ij}^{k} + \frac{\Delta t}{h}\left[ r_{ij} - s_{ij}^{k} - b_{ij}^{k+1} - \beta\left( \nabla_x^{-} \frac{\nabla_x^{+} s_{ij}^{k}}{\sqrt{\varepsilon + (\nabla_x^{+} s_{ij}^{k})^2 + (m(\nabla_y^{+} s_{ij}^{k}, \nabla_y^{-} s_{ij}^{k}))^2}} + \nabla_y^{-} \frac{\nabla_y^{+} s_{ij}^{k}}{\sqrt{\varepsilon + (\nabla_y^{+} s_{ij}^{k})^2 + (m(\nabla_x^{+} s_{ij}^{k}, \nabla_x^{-} s_{ij}^{k}))^2}} \right) \right] \tag{17}$$

Where,

$$t_k = k\Delta t,\ k = 0, 1, \ldots, b_{ij}^{k} = b(x_i, y_j, t_k),\ s_{ij}^{k} = s(x_i, y_j, t_k),\ m(\mathrm{a}, \mathrm{b}) = \left( \frac{sgn\ a + sgn\ b}{2} \right) min(|a|, |b|)$$

$h$ is the grid size. $\nabla_x{}^{-}$, $\nabla_y{}^{-}$, $\nabla_x{}^{+}$, $\nabla_x{}^{+}$ denote the backward (-) and forward (+) difference operators in the respective directions (x or y).

The iterations are continued till the normalized mean square error in $s$ and $b$ fall below predefined thresholds. The overall algorithm is summarized below;

**Algorithm 2.1.**

**Input:** Acquired image, $r$
**Initialization:** $b^0$ *is assumed as a Guassian low pass filtered version of* $r$ ; $s^0 = r$

**while** $\frac{\|b^{k+1}-b^k\|}{\|b^{k+1}\|} < \omega_b$ and $\frac{\|s^{k+1}-s^k\|}{\|s^{k+1}\|} < \omega_s$

1. Solve for $b^{k+1}$ using Eq. (15)
2. Normalize $b^{k+1}$
3. Solve for $s^{k+1}$ using Eq. (17)

**end while**
**Output:** Corrected image, $s$; bias field, $b$

Let the algorithm discussed above be referred to as 'the primitive method'. The implementation of the primitive method for intensity inhomogeneity correction in MR brain images as well as in some phantom images lead to some significant conclusions. Though minimization of TV norm was shown to be effective to maintain the uniform intensity levels, the weak edges were found to be diminished. The finer structure details in the brain images were observed to be over smoothed in the corrected image. This observation can be correlated to the results obtained by D. Dobson et al. [65] and Zhenghua Huang et al. [66] for denoising and illumination correction applications in natural images. Therefore, the current paper suggests a suitable replacement for TV norm in the view of preserving fine structures.

### 2.2. Sparsity constraint for true image in framelet domain

The ideal MR image can be regarded a piecewise constant image. Such images have a sparse representation under a tight framelet system that is highly redundant and offers high localization in spatial and frequency domains [67,68]. The redundant nature of the system also ensures robustness to noise [69]. Since framelet transform facilitates multi-resolution analysis, the multi-scale edge structures can be well captured [66,70]. Therefore, the current paper suggests framelet regularization as an alternative to TV norm regularization to effectively preserve details in the image.

The analysis and synthesis operators of the framelet transform are realized by a set of filters associated with the tight framelet system constructed via unitary extension principle [68]. Here, the piecewise linear B-spline framelet system is considered. The filters considered are as follows;

$$h_0 = \frac{1}{4}[1,2,1];\ h_1 = \frac{\sqrt{2}}{4}[1,0,-1];\ h_2 = \frac{1}{4}[-1,2,-1] \tag{18}$$

A detailed formulation of the decomposition matrix $W$ of the above framelet system without downsampling under the Neumann boundary condition [70] is provided in the appendix. The primitive energy minimization formulation is updated by replacing the TV regularization as given below.

$$\arg\min_{s,b} E(s,b) = \arg\min_{s,b} \|r - s - b\|_2^2 + \alpha \|\nabla b\|_2^2 + \beta \|Ws\|_1 \tag{19}$$

The above energy minimization formulation seeks the sparsest solution in the framelet domain which is ultimately the piecewise constant corrected image. Since the above energy minimization problem is not jointly convex with respect to $s$ and $b$, alternating minimization is utilized and the associated sub-problems with respect to the unknown variables are formulated as below.

$b$ sub-problem

$$b^{k+1} = \arg\min_{b} \|r - s^k - b\|_2^2 + \alpha \|\nabla b\|_2^2 \tag{20}$$

$s$ sub-problem

$$s^{k+1} = \arg\min_{s} \|r - s - b^{k+1}\|_2^2 + \beta \|Ws\|_1 \tag{21}$$

The above sub-problems can be solved more efficiently using other numerical algorithms compared to time marching strategy. During the experimental analysis of the primitive method, the time marching for solving the sub-problems was found to be slowly convergent when step size restrictions [64] were imposed for stability. Therefore, a more efficient numerical algorithm is considered here for solving the sub-problems. Since the $b$ sub-problem is a differentiable optimization problem, the optimality condition obtained from the associated Euler-Langrange equation can be solved easily by using Fourier transform as follows;

$$b^{k+1} = \mathscr{F}^{-1}\left(\frac{\mathscr{F}(r - s^k)}{\mathscr{F}(1 + \alpha(\mathscr{F}^*(\nabla_h)\mathscr{F}(\nabla_h) + \mathscr{F}^*(\nabla_v)\mathscr{F}(\nabla_v)))}\right) \tag{22}$$

where $\nabla_h$ and $\nabla_v$ are the gradient operators in horizontal and vertical directions and $\mathscr{F}$, $\mathscr{F}^{-1}$ and $\mathscr{F}^*$ represent the Fourier transform, its inverse and complex conjugate respectively. Thus the $b$ sub-problem can be solved computationally efficiently. Whereas, the coupling between the $L_1$ term and the $L_2$ term in the $s$ sub-problem makes it hard to solve. And moreover, the $s$ sub-problem doesn't have a closed form solution and hence has to be solved iteratively. This difficulty can be overcome by introducing auxiliary variables [71,72]. In the works of Jian-Feng Cai et al. [73], Houzhang Fang et al. [74] and Yi chang et al. [75], it was shown that Split Bregman algorithm was powerful in solving framelet $L_1$ regularization problems for image restoration applications such as noise removal, deblurring, destripping etc. [70,73,74]. The decoupling of the $L_1$ regularization problem in Split Bregman algorithm is realized by introducing an auxiliary variable. Accordingly, Split Bregman is utilized here to decouple the terms in the $s$ subproblem as follows,

$$\arg\min_{s} \|r - s - b^{k+1}\|_2^2 + \beta \|d\|_1 \ s.t.\ d = Ws \tag{23}$$

The above constrained problem is converted to unconstrained by adding an $L_2$ penalty term and is rewritten as follows;

$$\arg\min_{s} \|r - s - b^{k+1}\|_2^2 + \beta \|d\|_1 + \lambda \|d - Ws - b_1\|_2^2 \tag{24}$$

where, $b_1$ is the Bregman parameter and $\lambda$ is positive. An alternating minimization scheme can be used solve to the above formulation. The sub-problem of Eq. (24) with respect to $s$ is differentiable and the optimality condition of the same obtained using Euler-Lagrange equation has a closed form solution as given below;

$$s^{k+1} = (1 + \lambda)^{-1}(r - b^{k+1} + \lambda\, W^{-1}(d^k - b_1^k)) \tag{25}$$

where, $W^{-1}$ is the inverse transform of $W$. The auxiliary variable $d$ in the above problem is updated by using shrinkage operator as follows;

$$d^{k+1} = shrink\left(Ws^{k+1} + b_1^k, \frac{\beta}{\lambda}\right) \tag{26}$$

$$where,\quad shrink(X,\theta) = max\{abs(X) - \theta, 0\}\ sign(X) \tag{27}$$

The Bregman variable is updated in the iterative scheme as follows;

$$b_1^{k+1} = b_1^k + (Ws^{k+1} - d^{k+1}) \tag{28}$$

Therefore, the iterative strategy for solving the energy minimization problem defined in Eq. (19) is summarized below;

**Algorithm 2.2.**

**Input:** Acquired image, $r$

**Initialization:** $b^0$ *is assumed as a Guassian low pass filtered version of* $r$; $s^0 = r$; $d^0 = 0$; $b_1^0 = 0$

**while** $\frac{\|b^{k+1} - b^k\|}{\|b^{k+1}\|} < \omega_b$ and $\frac{\|s^{k+1} - s^k\|}{\|s^{k+1}\|} < \omega_s$

1. Solve for $b^{k+1}$ using $b^{k+1} = F^{-1}\left(\frac{F(r - s^k)}{F(1 + \alpha(F^*(\nabla_h)F(\nabla_h) + F^*(\nabla_v)F(\nabla_v)))}\right)$
2. Normalize $b^{k+1}$
3. Solve for $s^{k+1}$ using $s^{k+1} = (1 + \lambda)^{-1}(r - b^{k+1} + \lambda\, W^{-1}(d^k - b_1^k))$
4. Solve for $d^{k+1}$ using $d^{k+1} = shrink\left(Ws^{k+1} + b_1^k, \frac{\beta}{\lambda}\right)$
5. Update $b_1^{k+1}$ using $b_1^{k+1} = b_1^k + (Ws^{k+1} - d^{k+1})$

**end while**

**Output:** Corrected image, $s$; bias field, $b$

It is observed from the experimental analyses of Algorithm 2.2 that the application of framelet regularizer assisted to preserve the small scale edges better compared to TV norm regularizer. Fig. 1 compares the magnitude of the gradient map obtained by applying Sobel edge detector on the corrected images from both regularization strategies. It is evident that the small scale edges and details in the corrected image are over-smoothed when using TV regularizer whereas framelet regularizer preserves the same. This is because edges and finer details in the image lead to larger framelet coefficients and are preserved well during the $L_1$ norm minimization [76].

Despite the finding that the finer details edges were preserved in the

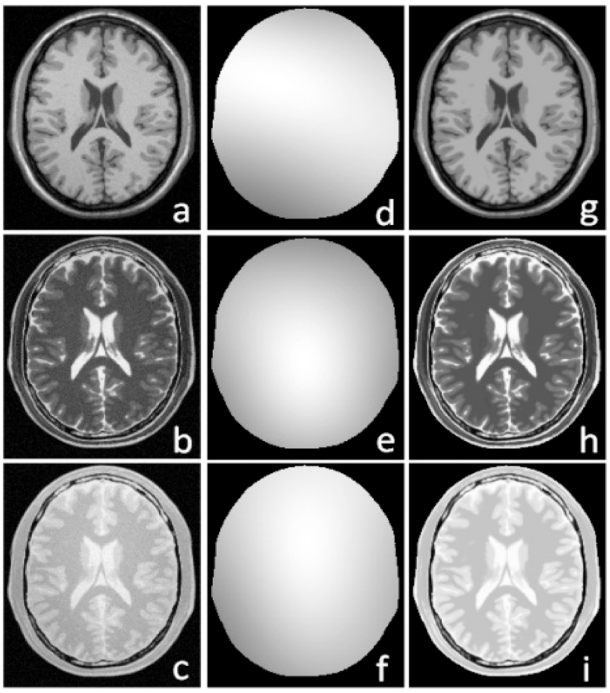


**Fig. 2.** Intensity inhomogeneity correction on simulated data. [a–c] T1-w, T2-w, PD original images (3% noise, 40%intensity inhomogeneity), [d–f] Estimated bias fields of [a–c], [g–i] Corrected images of [a–c].

corrected image, the bias field obtained was not found to be smooth as desired. Alternatively, the degree of smoothness possible for bias field via penalizing the $L_2$ norm was not found to be satisfactory. It is also evident in the results obtained by Yuping Duan et al. [77] and Xi Chen et al. [63] for bias field estimation in MR images. Therefore, the paper proposes an efficient replacement for the $L_2$ norm penalization to estimate the smooth bias field without constraining to any specific parametric model.

### 2.3. Sparsity constraint for bias field in Fourier domain

The bias field is smoothly varying in spatial domain and hence has dominant low frequency spectrum. Therefore, it is reasonable to assume a sparse representation for bias field in the Fourier domain. Thus the optimization problem aims to decompose the acquired image into a piecewise constant image and a bias field that are approximated to be sparse in framelet and Fourier domain respectively. The sparse constraint in Fourier domain regulates the smoothness of the bias field and is realized by regulating the $L_1$ norm of the Fourier transform of bias field. The intensity inhomogeneity problem is expressed as a constrained minimization problem as follows;

$$\arg\min_{s,b} \|Ws\|_1 + \alpha \|\mathcal{F}(b)\|_1 \; s.t. \; r = s + b \tag{29}$$

where, $\mathcal{F}(b)$ represents the Fourier transform of the bias field. The minimization problem is solved using the linearized augmented Lagrangian method [78] which linearizes the quadratic term penalty term added in the alternating direction method while solving the sub-problems. The linearization eliminates the necessity for auxiliary variables thereby reducing the computational complexity in updating them. In addition, convergence is relatively faster without the auxiliary variables [78]. The Linearized Augmented Lagrangian function of the above problem Eq. (29) is written as follows;

$$L(b,s;Y,\mu) = \|Ws\|_1 + \alpha \|\mathcal{F}(b)\|_1 + \langle Y, r-s-b\rangle + \mu \|r-s-b\|_F \tag{30}$$

where, $Y$ denotes the Lagrangian multiplier. $\|\cdot\|_F$ is the Frobenius norm and the penalty parameter $\mu > 0$. The functional $L$ in Eq. (30) can be split into different sub-problems. The sub-problem to solve $b^{k+1}$ is given below;

$$b^{k+1} = \arg\min_b L(b, s^k, Y^k, \mu^k) \tag{31}$$

$$\arg\min_b L(s^k, b, Y^k, \mu^k) = \arg\min_b \alpha \|\mathcal{F}(b)\|_1 + \langle Y, r-s-b\rangle + \mu^k \|r-s-b\|_F \tag{32}$$

Eq. (32) leads to the following closed form solution easily:

$$\mathcal{F}(b^{k+1}) = Shrink\left(\mathcal{F}(b^k) + \mathcal{F}(r - s^k - b^k + Y^k/\mu^k), \frac{\alpha}{\mu^k}\right) \tag{33}$$

$$b^{k+1} = \mathcal{F}^{-1}(b^{k+1}) \tag{34}$$

The $s$ sub-problem that solves to obtain $s^{k+1}$ is given below;

$$\arg\min_s L(s, b^{k+1}, Y^k, \mu^k) = \arg\min_s \|Ws\|_1 + \langle Y^k, r-s-b^{k+1}\rangle + \mu^k \|r-s-b^{k+1}\|_F \tag{35}$$

The above sub-problem in Eq. (35) is solved to obtain the following solution:

$$Temp = Shrink\left(Ws^k + W(r - s^k - b^{k+1} + Y^k/\mu^k), \frac{1}{\mu^k}\right) \tag{36}$$

$$s^{k+1} = W^{-1}\, Temp \tag{37}$$

where, *Temp* is a temporary variable. The Lagrangian and the penalty parameters are updated as shown below:

$$Y^{k+1} = Y^k + \mu^k(r - s^{k+1} - b^{k+1}) \tag{38}$$

$$\mu^{k+1} = \rho\, \mu^k \tag{39}$$

The algorithm iterates between the sub-problems until a predefined criteria is satisfied. Finally, the bias field and the corrected images are obtained after taking the exponential of the optimal solutions for $b$ and $s$ repsectively. The iterative algorithm is summarized below;

**Algorithm 2.3.**

**Input:** Acquired image, $r$

**Initialization:** $b^0$ *is assumed as a Guassian low pass filtered version of* $r$; $s^0 = r; Y^0 = 0;\ \mu^0 > 0$

**while** $\frac{\|b^{k+1}-b^k\|}{\|b^{k+1}\|} < \omega_b$ and $\frac{\|s^{k+1}-s^k\|}{\|s^{k+1}\|} < \omega_s$

1. $\mathcal{F}(b^{k+1}) = Shrink\left(\mathcal{F}(b^k) + \mathcal{F}(r - s^k - b^k + Y^k/\mu^k), \frac{\alpha}{\mu^k}\right)$
2. $b^{k+1} = \mathcal{F}^{-1}(b^{k+1})$
3. Normalize $b^{k+1}$
4. $Temp = Shrink\left(Ws^k + W(r - s^k - b^{k+1} + Y^k/\mu^k), \frac{1}{\mu^k}\right)$
5. $s^{k+1} = W^{-1}\, Temp$
6. Update $Y^{k+1}$ using $Y^{k+1} = Y^k + \mu^k(r - s^{k+1} - b^{k+1})$
7. Update $\mu^{k+1}$ using $\mu^{k+1} = \rho\, \mu^k$

**end while**

**Output:** Corrected image, $s$; bias field, $b$

The proposed algorithm optimizes the corrected image and the bias field iteratively according to the Linearized Augmented Lagrangian method updating scheme. The algorithm seeks the sparse solutions for $s$ and $b$ in Framelet and Fourier domains respectively through $L_1$ minimization. The sparse solution obtained in Fourier domain for $b$ can effectively achieve desired smoothness in the spatial domain without constraining to any parametric model. Hence the proposed methodology eliminates necessity for predefined parameters that critically control the degree of smoothness.

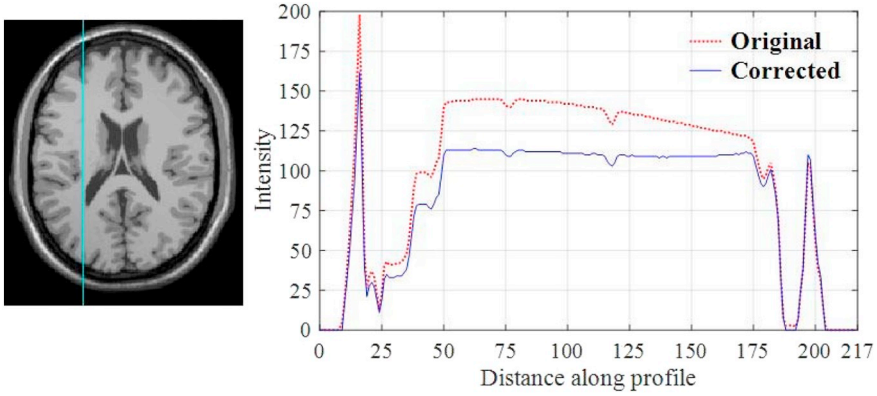


**Fig. 3.** Comparison of intensity profiles. Intensity profiles before and after the correction of an axial T1-w image (0% noise, 40% intensity inhomogeneity) along a selected line marked in turquoise color. (For interpretation of the references to color in this figure legend, the reader is referred to the web version of this article.)

**Table 1**
CV values in grey matter on T1-w axial images.

| Noise level (%) | Bias field (%) | Original | N4 | LSACM | MICO | IACM | Proposed | NIMS | MFCM |
|---|---|---|---|---|---|---|---|---|---|
| 1 | 20 | 9.66 ± 0.38 | 9.14 ± 0.36 | 9.23 ± 0.68 | 9.19 ± 1.86 | 9.13 ± 0.58 | 9.11 ± 0.43 | 9.12 ± 0.61 | 9.33 ± 0.81 |
| | 40 | 10.86 ± 0.39 | 9.19 ± 0.35 | 9.32 ± 0.90 | 9.22 ± 1.66 | 9.27 ± 0.79 | 9.23 ± 0.64 | 9.18 ± 0.55 | 9.38 ± 0.78 |
| | 60 | 12.36 ± 0.40 | 9.58 ± 0.33 | 9.67 ± 1.01 | 9.61 ± 0.98 | 9.60 ± 0.71 | 9.56 ± 0.60 | 9.57 ± 0.63 | 9.69 ± 0.99 |
| | 80 | 13.95 ± 0.41 | 9.83 ± 0.39 | 9.88 ± 0.67 | 9.75 ± 1.07 | 9.68 ± 0.93 | 9.69 ± 0.65 | 9.81 ± 0.72 | 9.85 ± 0.79 |
| 5 | 20 | 11.71 ± 0.32 | 11.27 ± 0.31 | 11.35 ± 0.48 | 11.25 ± 1.07 | 11.23 ± 0.69 | 11.21 ± 0.72 | 11.25 ± 0.74 | 11.37 ± 0.87 |
| | 40 | 12.72 ± 0.34 | 11.30 ± 0.31 | 11.40 ± 0.42 | 11.28 ± 0.95 | 11.29 ± 0.83 | 11.27 ± 0.60 | 11.29 ± 0.65 | 11.45 ± 0.81 |
| | 60 | 14.03 ± 0.35 | 11.41 ± 0.31 | 11.59 ± 0.44 | 11.47 ± 0.90 | 11.38 ± 0.86 | 11.34 ± 0.61 | 11.40 ± 0.88 | 11.58 ± 0.99 |
| | 80 | 15.45 ± 0.36 | 11.73 ± 0.31 | 11.90 ± 0.45 | 11.81 ± 1.08 | 11.72 ± 0.68 | 11.71 ± 0.72 | 11.78 ± 0.89 | 11.89 ± 0.77 |
| 9 | 20 | 15.37 ± 0.27 | 15.10 ± 0.27 | 15.24 ± 0.66 | 15.27 ± 0.99 | 15.05 ± 0.71 | 15.04 ± 0.64 | 15.07 ± 0.61 | 15.25 ± 0.81 |
| | 40 | 16.17 ± 0.29 | 15.24 ± 0.27 | 15.31 ± 0.53 | 15.48 ± 0.99 | 15.18 ± 0.88 | 15.15 ± 0.68 | 15.22 ± 0.70 | 15.34 ± 0.62 |
| | 60 | 17.22 ± 0.30 | 15.50 ± 0.27 | 16.64 ± 0.43 | 16.67 ± 0.95 | 15.45 ± 0.70 | 15.43 ± 0.61 | 15.52 ± 0.63 | 15.75 ± 0.64 |
| | 80 | 18.41 ± 0.32 | 15.87 ± 0.28 | 16.68 ± 0.38 | 16.90 ± 0.92 | 15.67 ± 0.98 | 15.63 ± 0.71 | 15.75 ± 0.74 | 15.73 ± 0.71 |

**Table 2**
CV values in white matter on T1-w axial images.

| Noise level (%) | Bias field (%) | Original | N4 | LSACM | MICO | IACM | Proposed | NIMS | MFCM |
|---|---|---|---|---|---|---|---|---|---|
| 1 | 20 | 5.19 ± 0.37 | 4.14 ± 0.48 | 4.31 ± 0.62 | 4.20 ± 0.69 | 4.10 ± 1.01 | 4.11 ± 0.61 | 4.12 ± 0.58 | 4.25 ± 0.92 |
| | 40 | 6.81 ± 0.41 | 4.18 ± 0.45 | 4.38 ± 1.04 | 4.26 ± 0.54 | 4.15 ± 0.98 | 4.14 ± 0.62 | 4.15 ± 0.65 | 4.40 ± 0.89 |
| | 60 | 8.53 ± 0.69 | 4.48 ± 0.38 | 4.62 ± 1.13 | 4.43 ± 0.74 | 4.40 ± 0.94 | 4.42 ± 0.56 | 4.46 ± 0.70 | 4.68 ± 0.73 |
| | 80 | 10.17 ± 1.02 | 5.05 ± 0.37 | 5.12 ± 0.82 | 5.00 ± 0.88 | 5.04 ± 0.12 | 5.02 ± 0.71 | 5.04 ± 0.72 | 5.12 ± 0.98 |
| 5 | 20 | 7.24 ± 0.32 | 6.50 ± 0.33 | 6.71 ± 0.70 | 6.63 ± 0.71 | 6.44 ± 0.69 | 6.46 ± 0.60 | 6.48 ± 0.53 | 6.74 ± 0.73 |
| | 40 | 8.49 ± 0.35 | 6.51 ± 0.32 | 6.65 ± 0.73 | 6.60 ± 0.58 | 6.47 ± 0.79 | 6.47 ± 0.58 | 6.50 ± 0.55 | 6.64 ± 0.84 |
| | 60 | 9.92 ± 0.59 | 6.57 ± 0.29 | 6.86 ± 0.49 | 6.88 ± 0.53 | 6.51 ± 0.81 | 6.50 ± 0.59 | 6.53 ± 0.67 | 6.88 ± 0.52 |
| | 80 | 11.37 ± 0.89 | 6.79 ± 0.25 | 6.89 ± 0.73 | 6.90 ± 0.76 | 6.68 ± 0.75 | 6.67 ± 0.52 | 6.75 ± 0.55 | 6.91 ± 0.62 |
| 9 | 20 | 10.54 ± 0.31 | 10.08 ± 0.30 | 10.17 ± 0.57 | 10.25 ± 0.57 | 10.05 ± 1.01 | 10.07 ± 0.64 | 10.06 ± 0.58 | 10.21 ± 0.68 |
| | 40 | 11.44 ± 0.31 | 10.17 ± 0.29 | 10.28 ± 0.36 | 10.34 ± 0.56 | 10.15 ± 0.89 | 10.14 ± 0.69 | 10.15 ± 0.61 | 10.23 ± 0.73 |
| | 60 | 12.55 ± 0.46 | 10.36 ± 0.28 | 10.40 ± 0.34 | 10.63 ± 0.52 | 10.27 ± 0.81 | 10.2 ± 0.78 | 10.31 ± 0.64 | 10.41 ± 0.58 |
| | 80 | 13.74 ± 0.71 | 10.65 ± 0.27 | 10.56 ± 0.43 | 10.61 ± 0.49 | 10.40 ± 0.75 | 10.39 ± 0.72 | 10.42 ± 0.88 | 10.59 ± 0.54 |

**Table 3**
CV values in grey matter on T2-w axial images.

| Noise level (%) | Bias field (%) | Original | N4 | LSACM | MICO | IACM | Proposed | NIMS | MFCM |
|---|---|---|---|---|---|---|---|---|---|
| 1 | 20 | 16.41 ± 0.51 | 16.37 ± 0.56 | 16.41 ± 0.81 | 16.40 ± 0.71 | 16.33 ± 0.32 | 16.32 ± 0.43 | 16.35 ± 0.66 | 16.43 ± 0.45 |
| | 40 | 16.77 ± 0.48 | 16.31 ± 0.57 | 16.73 ± 0.75 | 16.48 ± 0.65 | 16.30 ± 0.46 | 16.34 ± 0.51 | 16.36 ± 0.62 | 16.68 ± 0.32 |
| | 60 | 17.35 ± 0.54 | 16.41 ± 0.55 | 16.91 ± 0.89 | 16.50 ± 0.62 | 16.41 ± 0.44 | 16.38 ± 0.48 | 16.40 ± 0.60 | 16.93 ± 0.62 |
| | 80 | 18.06 ± 0.73 | 16.74 ± 0.52 | 18.00 ± 0.63 | 16.77 ± 0.60 | 16.76 ± 0.56 | 16.70 ± 0.49 | 16.72 ± 0.58 | 17.98 ± 0.72 |
| 5 | 20 | 19.68 ± 0.37 | 19.62 ± 0.40 | 19.67 ± 0.50 | 19.66 ± 0.68 | 19.65 ± 0.62 | 19.60 ± 0.58 | 19.63 ± 0.62 | 19.64 ± 1.05 |
| | 40 | 19.98 ± 0.38 | 19.58 ± 0.41 | 19.97 ± 0.54 | 19.73 ± 0.62 | 19.65 ± 0.65 | 19.60 ± 0.57 | 19.64 ± 0.57 | 19.89 ± 0.78 |
| | 60 | 20.48 ± 0.48 | 19.69 ± 0.39 | 20.45 ± 1.04 | 20.02 ± 0.55 | 19.71 ± 0.55 | 19.64 ± 0.63 | 19.65 ± 0.54 | 20.38 ± 0.61 |
| | 80 | 21.10 ± 0.67 | 20.00 ± 0.37 | 21.03 ± 1.06 | 20.33 ± 0.49 | 20.05 ± 0.63 | 19.93 ± 0.46 | 19.92 ± 0.51 | 20.42 ± 0.51 |
| 9 | 20 | 25.40 ± 0.31 | 25.33 ± 0.32 | 25.41 ± 0.21 | 25.39 ± 0.41 | 25.37 ± 0.87 | 25.09 ± 0.71 | 25.12 ± 0.82 | 25.44 ± 0.84 |
| | 40 | 25.64 ± 0.34 | 25.32 ± 0.32 | 25.63 ± 1.17 | 25.63 ± 0.39 | 25.38 ± 0.79 | 25.15 ± 0.68 | 25.20 ± 0.78 | 25.60 ± 1.08 |
| | 60 | 26.05 ± 0.44 | 25.44 ± 0.31 | 25.89 ± 0.89 | 25.91 ± 0.37 | 25.42 ± 0.68 | 25.32 ± 0.59 | 25.38 ± 0.75 | 25.88 ± 0.91 |
| | 80 | 26.55 ± 0.61 | 25.70 ± 0.32 | 25.92 ± 0.60 | 25.80 ± 0.36 | 25.68 ± 0.83 | 25.35 ± 0.81 | 25.40 ± 0.71 | 25.97 ± 0.87 |

**Table 4**
CV values in white matter on T2-w axial images.

| Noise level (%) | Bias field (%) | Original | N4 | LSACM | MICO | IACM | Proposed | NIMS | MFCM |
|---|---|---|---|---|---|---|---|---|---|
| 1 | 20 | 7.46 ± 0.79 | 7.26 ± 0.49 | 7.40 ± 0.47 | 7.28 ± 0.52 | 7.25 ± 0.70 | 7.27 ± 0.67 | 7.26 ± 0.81 | 7.38 ± 0.89 |
| | 40 | 8.09 ± 1.14 | 7.31 ± 0.69 | 7.59 ± 0.68 | 7.38 ± 0.38 | 7.26 ± 0.64 | 7.25 ± 0.75 | 7.28 ± 0.84 | 7.98 ± 0.83 |
| | 60 | 8.92 ± 1.48 | 7.54 ± 0.92 | 7.85 ± 2.71 | 7.55 ± 0.31 | 7.47 ± 0.71 | 7.45 ± 0.77 | 7.48 ± 0.83 | 8.12 ± 0.83 |
| | 80 | 9.85 ± 1.81 | 8.12 ± 1.26 | 8.96 ± 2.90 | 8.36 ± 0.30 | 8.16 ± 0.84 | 8.06 ± 0.81 | 8.09 ± 0.87 | 8.16 ± 0.87 |
| 5 | 20 | 17.61 ± 0.23 | 17.46 ± 0.27 | 17.51 ± 0.85 | 17.58 ± 0.64 | 17.48 ± 0.90 | 17.45 ± 0.55 | 17.44 ± 0.45 | 17.99 ± 0.45 |
| | 40 | 17.91 ± 0.36 | 17.46 ± 0.25 | 17.77 ± 1.13 | 17.66 ± 0.58 | 17.51 ± 0.87 | 17.41 ± 0.76 | 17.40 ± 0.43 | 17.98 ± 0.43 |
| | 60 | 18.33 ± 0.55 | 17.60 ± 0.30 | 17.84 ± 0.96 | 18.07 ± 0.52 | 17.64 ± 0.69 | 17.50 ± 0.48 | 17.52 ± 0.42 | 17.99 ± 0.42 |
| | 80 | 18.83 ± 0.78 | 17.90 ± 0.43 | 18.51 ± 0.98 | 17.99 ± 0.46 | 17.95 ± 1.01 | 17.84 ± 0.59 | 17.87 ± 0.40 | 17.99 ± 0.40 |
| 9 | 20 | 28.61 ± 0.40 | 28.52 ± 0.44 | 28.58 ± 1.20 | 28.60 ± 0.56 | 28.50 ± 0.89 | 28.51 ± 0.63 | 28.55 ± 0.70 | 28.59 ± 0.63 |
| | 40 | 28.81 ± 0.42 | 28.54 ± 0.43 | 28.68 ± 0.72 | 28.78 ± 0.54 | 28.58 ± 0.62 | 28.50 ± 0.82 | 28.56 ± 0.61 | 28.68 ± 0.72 |
| | 60 | 29.08 ± 0.48 | 28.64 ± 0.45 | 28.75 ± 0.64 | 28.79 ± 0.49 | 28.70 ± 0.98 | 28.58 ± 0.61 | 28.60 ± 0.59 | 28.98 ± 0.56 |
| | 80 | 29.42 ± 0.59 | 28.83 ± 0.50 | 29.11 ± 0.58 | 28.85 ± 0.51 | 28.79 ± 0.92 | 28.76 ± 0.63 | 28.78 ± 0.58 | 29.08 ± 0.88 |

**Table 5**
CV values in grey matter on PD axial images.

| Noise level (%) | Bias field (%) | Original | N4 | LSACM | MICO | IACM | Proposed | NIMS | MFCM |
|---|---|---|---|---|---|---|---|---|---|
| 1 | 20 | 4.14 ± 0.19 | 3.35 ± 0.18 | 3.86 ± 0.31 | 3.91 ± 0.56 | 3.37 ± 0.09 | 3.34 ± 0.12 | 3.33 ± 0.15 | 3.88 ± 0.22 |
| | 40 | 6.09 ± 0.51 | 3.47 ± 0.19 | 3.87 ± 0.17 | 3.99 ± 0.54 | 3.41 ± 0.12 | 3.42 ± 0.10 | 3.44 ± 0.18 | 3.86 ± 0.20 |
| | 60 | 8.11 ± 0.83 | 3.60 ± 0.20 | 3.88 ± 0.17 | 4.01 ± 0.55 | 3.56 ± 0.17 | 3.55 ± 0.14 | 3.58 ± 0.19 | 3.87 ± 0.19 |
| | 80 | 10.03 ± 1.15 | 3.71 ± 0.21 | 3.89 ± 0.39 | 4.09 ± 0.57 | 3.56 ± 0.18 | 3.57 ± 0.11 | 3.58 ± 0.25 | 3.87 ± 0.20 |
| 5 | 20 | 6.96 ± 0.12 | 6.68 ± 0.14 | 6.80 ± 0.11 | 6.80 ± 0.25 | 6.62 ± 0.20 | 6.62 ± 0.15 | 6.63 ± 0.18 | 6.82 ± 0.16 |
| | 40 | 8.28 ± 0.37 | 6.71 ± 0.15 | 6.81 ± 0.17 | 6.83 ± 0.21 | 6.63 ± 0.19 | 6.61 ± 0.18 | 6.64 ± 0.20 | 6.83 ± 0.17 |
| | 60 | 9.87 ± 0.67 | 6.71 ± 0.15 | 6.80 ± 0.12 | 6.85 ± 0.19 | 6.67 ± 0.21 | 6.64 ± 0.19 | 6.65 ± 0.12 | 6.85 ± 0.14 |
| | 80 | 11.51 ± 0.98 | 6.78 ± 0.12 | 6.81 ± 0.21 | 6.89 ± 0.17 | 6.70 ± 0.16 | 6.65 ± 0.14 | 6.68 ± 0.13 | 6.88 ± 0.24 |
| 9 | 20 | 10.97 ± 0.13 | 10.78 ± 0.12 | 10.86 ± 0.12 | 10.88 ± 0.22 | 10.73 ± 0.11 | 10.74 ± 0.09 | 10.76 ± 0.14 | 10.89 ± 0.19 |
| | 40 | 11.86 ± 0.29 | 10.82 ± 0.14 | 10.86 ± 0.11 | 10.91 ± 0.18 | 10.75 ± 0.19 | 10.75 ± 0.12 | 10.80 ± 0.15 | 10.91 ± 0.21 |
| | 60 | 13.03 ± 0.53 | 10.89 ± 0.16 | 10.87 ± 0.16 | 10.91 ± 0.16 | 10.76 ± 0.21 | 10.78 ± 0.14 | 10.81 ± 0.18 | 10.96 ± 0.18 |
| | 80 | 14.33 ± 0.81 | 10.96 ± 0.12 | 10.88 ± 0.15 | 10.93 ± 0.14 | 10.82 ± 0.14 | 10.81 ± 0.18 | 10.82 ± 0.16 | 10.98 ± 0.23 |

## 3. Results and discussion

The performance of the proposed methodology was extensively evaluated on simulated and real brain datasets. The results were qualitatively analyzed by an expert radiologist. The performance of the algorithm was compared with our previous approach, NIMS [13], an FCM based methodology proposed by Ahmed et al. [79] addressed as 'MFCM', N4 method [23] and some recent retrospective correction methods such as MICO [22] by Li et al., LSACM by Zhang et al. [30] and an improved active contour method by Meng et al. addressed as 'IACM' [46].

The efficacy of the proposed methodology was evaluated through various quantitative measures which include coefficient of variation (CV) and coefficient of joint variation (CJV). An efficient intensity inhomogeneity correction method is expected to reduce the intra-class intensity variations while improving the inter-class intensity separation. Coefficient of variation is a measure of the intra-class tissue intensity variations alone and coefficient of joint variation provides details on the inter-class separation. Here, both the measures are calculated with respect to two distinct tissue regions $S_1$ (grey matter) and $S_2$ (white matter) and are defined as follows,

$$CV(S_i) = \frac{\sigma(S_i)}{\mu(S_i)} \; i = 1, 2 \tag{40}$$

$$CJV(S_1, S_2) = \frac{\sigma(S_1) + \sigma(S_2)}{|\mu(S_1) - \mu(S_2)|} \tag{41}$$

$\mu$ and $\sigma$ represent the mean and standard deviation of tissue class respectively. The quantitative results are assessed when the algorithm was run on a Windows system with 4GB RAM and Pentium(R) dual-core 2.2GHz processor in MATLAB 2016a.

### 3.1. BrainWeb simulated database

The BrainWeb database[1] [80] offers brain dataset generated through an MRI simulator. The performance of the proposed methodology was evaluated on BrainWeb datasets of T1-w, T2-w and PD modality volumes of 181 × 217 × 181 dimensions with 1 mm slice thickness. The ground truth segmentations are also available in the database and were utilized for quantitative analysis.

The analysis was made for results obtained with 2D images of T1-w, T2-w and PD modalities corrupted by 20%, 40%, 60% and 80% levels of intensity inhomogeneity. The intensity inhomogeneity was introduced in the images utilizing three different reference bias fields provided in the dataset fields namely field A, field B and field C and were multiplied to T1-w, T2-w and PD volumes respectively.

The intensity inhomogeneity corrected images obtained after the application of the proposed methodology on three different modality images are provided in Fig. 2. The first column of Fig. 2 shows the original axial mid-slices of T1-w, T2-w and PD with 3% noise level degraded by 40% intensity inhomogeneity. The second and third columns of the same figure display the estimated bias field and final corrected images of the corresponding original images shown in the first column.

The tissue regions in the corrected images of Fig. 2 appear to be more uniform in the intensity level in visual analysis after the application of the proposed methodology which indicates a better correction of the artificially introduced 40% inhomogeneity. The contrast between different tissue regions is also enhanced after intensity inhomogeneity correction which shows a reduction in the overlap of different tissue region intensity levels caused by bias field. Moreover, significant reduction in the noise is also evident which can be attributed to the sparseness constraint imposed in the framelet domain which has

[1] http://www.bic.mni.mcgill.ca/brainweb

**Table 6**
CV values in white matter on PD axial images.

| Noise level (%) | bias field (%) | Original | N4 | LSACM | MICO | IACM | Proposed | NIMS | MFCM |
|---|---|---|---|---|---|---|---|---|---|
| 1 | 20 | 3.72 ± 0.51 | 3.11 ± 0.21 | 3.69 ± 0.23 | 3.70 ± 0.48 | 3.06 ± 0.19 | 3.08 ± 0.26 | 3.12 ± 0.18 | 3.66 ± 0.19 |
| | 40 | 5.22 ± 0.97 | 3.12 ± 0.18 | 3.70 ± 0.24 | 3.78 ± 0.47 | 3.10 ± 0.22 | 3.12 ± 0.28 | 3.12 ± 0.21 | 3.71 ± 0.21 |
| | 60 | 6.84 ± 1.41 | 3.12 ± 0.21 | 3.70 ± 0.24 | 3.82 ± 0.49 | 3.18 ± 0.18 | 3.17 ± 0.29 | 3.13 ± 0.24 | 3.72 ± 0.16 |
| | 80 | 8.40 ± 1.81 | 3.14 ± 0.20 | 4.13 ± 0.54 | 3.92 ± 0.53 | 3.19 ± 0.19 | 3.18 ± 0.30 | 3.14 ± 0.17 | 4.09 ± 0.27 |
| 5 | 20 | 7.46 ± 0.25 | 7.26 ± 0.06 | 7.44 ± 0.18 | 7.44 ± 0.22 | 7.21 ± 0.13 | 7.22 ± 0.10 | 7.25 ± 0.10 | 7.38 ± 0.22 |
| | 40 | 8.34 ± 0.61 | 7.26 ± 0.08 | 7.44 ± 0.18 | 7.47 ± 0.19 | 7.22 ± 0.15 | 7.23 ± 0.11 | 7.26 ± 0.12 | 7.40 ± 0.21 |
| | 60 | 9.47 ± 1.03 | 7.27 ± 0.06 | 7.45 ± 0.18 | 7.48 ± 0.17 | 7.25 ± 0.14 | 7.25 ± 0.11 | 7.26 ± 0.09 | 7.42 ± 0.15 |
| | 80 | 10.67 ± 1.44 | 7.28 ± 0.09 | 7.70 ± 0.31 | 7.48 ± 0.16 | 7.26 ± 0.11 | 7.27 ± 0.12 | 7.27 ± 0.14 | 7.45 ± 0.25 |
| 9 | 20 | 12.29 ± 0.19 | 12.16 ± 0.12 | 12.27 ± 0.19 | 12.27 ± 0.21 | 12.11 ± 0.21 | 12.16 ± 0.14 | 12.15 ± 0.12 | 12.25 ± 0.21 |
| | 40 | 12.86 ± 0.42 | 12.16 ± 0.15 | 12.28 ± 0.19 | 12.34 ± 0.19 | 12.12 ± 0.19 | 12.17 ± 0.16 | 12.15 ± 0.15 | 12.26 ± 0.22 |
| | 60 | 13.64 ± 0.73 | 12.17 ± 0.16 | 12.28 ± 0.19 | 12.32 ± 0.17 | 12.15 ± 0.20 | 12.17 ± 0.14 | 12.16 ± 0.18 | 12.26 ± 0.19 |
| | 80 | 14.52 ± 1.07 | 12.18 ± 0.19 | 12.31 ± 0.27 | 12.40 ± 0.15 | 12.19 ± 0.17 | 12.19 ± 0.14 | 12.16 ± 0.20 | 12.29 ± 0.20 |

already proven to be effective in suppressing random noise [76].

It is observed from Fig. 2 that the estimated bias fields are smooth surfaces that do not contain any anatomical details of the input images. This directs to the efficacy in estimating bias field by approximating a sparse representation in the Fourier domain. It is also worth to note that the edges of the input images are well preserved in the corrected images which could be attributed to the sparsity constraint imposed in the framelet domain. This is due to preservation of the larger framelet coefficients corresponding to edges and finer details during the $L_1$ norm minimization. The advantages of sparsity constraint in the framelet domain is twofold; it helps to recover the piecewise constant image and also aids in noise removal.

The improved homogeneity in white matter tissue region after the correction strategy is evident in the intensity profile plot given in Fig. 3. The figure plots the intensity profiles along the selected line marked in turquoise color, before and after correction in the simulated T1-w axial image with 0% noise and 40% intensity inhomogeneity. The intensity in the white matter region along the selected line in the original image varies smoothly due to intensity inhomogeneity so that the maximum intensity variation in white matter region (between 50 and 175 along the x-axis) is around 25. This variation in the intensity with respect to location has disappeared after the correction and the intensity level is consistent around 115, suggesting a good correction for intensity inhomogeneity. The singularities in the intensity at various distances indicate the presence of tissue region boundaries and are not affected by the correction. This clearly shows that the proposed correction strategy is effective for intensity inhomogeneity correction while preserving the edges and finer details in the input images.

The performance of the proposed scheme was compared against N4, LSACM, MICO, IACM, NIMS and MFCM quantitatively in terms of CV and CJV values. The comparison was made on original images at 20%, 40%, 60% and 80% intensity inhomogeneity levels for 1%, 3%, 5% and 9% noise levels. The comparison of CV values in Grey matter region before and after the correction by various methods is given in Tables 1, 3, 7 for T1-w, T2-w and PD data respectively. Tables 2, 4, 8 provide the comparison of CV in white matter tissue region on T1-w, T2-w and PD simulated data respectively. The axial slices containing > 1000 pixels were only considered for this CV calculation. The parameters for each method are set with the default values specified in the corresponding paper which are listed in Appendix B. The N4ITK bias field corrections were performed in the 3DSlicer software (https://www.slicer.org) which has an integrated N4 correction module.

It is clear from the Tables 1 to 6 that the CV values have been reduced when all the seven correction methods were applied. The overall performance of the proposed methodology is comparable to IACM, N4 and NIMS. But, N4 produced a moderate performance at higher noise levels. The performance of MICO at lower noise levels is comparable to N4. For all the cases considered in the tables, a significant reduction in the CV values has been observed for the proposed methodology indicating a good correction. This indicates that the proposed methodology reduces the intensity scatter in the white matter and grey matter regions significantly. It is also verified from the quantitative analyses that the methodology corrects for intensity inhomogeneity effectively irrespective of the image modality. Moreover, the methodology has maintained consistency in performance for distinct noise levels and has shown superior performance in most of the cases considered. Hence, the quantitative analysis in simulated brain data proves the efficacy of the proposed method under higher noise levels and bias field.

The CJV values are compared in reference to white matter and grey matter regions and are provided in Tables 7–9 respectively for T1-w, T2-w and PD BrainWeb simulated data. It depicts that the proposed methodology shows better performance in reducing the CJV values compared to the other algorithms considered. The considerable reduction in the CJV indicates an improved separation in the intensity levels of white matter and grey matter tissue regions. The same also amounts to the improved contrast observed in the corrected images which was already verified during the qualitative analysis. In some of the cases, MFCM and LSACM have shown to increase the CJV while offering lower

**Table 7**
Coefficient of joint variation on T1-w axial images of BrainWeb dataset.

| Noise level (%) | Bias field (%) | Original | N4 | LSACM | MICO | IACM | Proposed | NIMS | MFCM |
|---|---|---|---|---|---|---|---|---|---|
| 1 | 20 | 0.50 ± 0.03 | 0.46 ± 0.03 | 0.53 ± 0.11 | 0.45 ± 0.07 | 0.46 ± 0.04 | 0.45 ± 0.06 | 0.46 ± 0.04 | 0.51 ± 0.05 |
| | 40 | 0.59 ± 0.04 | 0.46 ± 0.03 | 0.61 ± 0.08 | 0.48 ± 0.05 | 0.44 ± 0.08 | 0.45 ± 0.04 | 0.46 ± 0.07 | 0.60 ± 0.09 |
| | 60 | 0.69 ± 0.06 | 0.48 ± 0.03 | 0.70 ± 0.09 | 0.53 ± 0.06 | 0.47 ± 0.03 | 0.47 ± 0.05 | 0.47 ± 0.06 | 0.71 ± 0.07 |
| | 80 | 0.79 ± 0.09 | 0.51 ± 0.03 | 0.80 ± 0.12 | 0.53 ± 0.12 | 0.51 ± 0.09 | 0.50 ± 0.10 | 0.51 ± 0.13 | 0.80 ± 0.09 |
| 5 | 20 | 0.65 ± 0.04 | 0.63 ± 0.03 | 0.68 ± 0.07 | 0.64 ± 0.08 | 0.61 ± 0.03 | 0.61 ± 0.04 | 0.63 ± 0.05 | 0.69 ± 0.06 |
| | 40 | 0.72 ± 0.04 | 0.63 ± 0.03 | 0.77 ± 0.06 | 0.64 ± 0.06 | 0.62 ± 0.04 | 0.62 ± 0.05 | 0.63 ± 0.04 | 0.75 ± 0.08 |
| | 60 | 0.80 ± 0.06 | 0.63 ± 0.04 | 0.86 ± 0.07 | 0.73 ± 0.12 | 0.64 ± 0.06 | 0.63 ± 0.04 | 0.64 ± 0.04 | 0.81 ± 0.09 |
| | 80 | 0.88 ± 0.09 | 0.64 ± 0.04 | 0.92 ± 0.06 | 0.74 ± 0.15 | 0.63 ± 0.05 | 0.62 ± 0.04 | 0.63 ± 0.02 | 0.89 ± 0.05 |
| 9 | 20 | 0.90 ± 0.05 | 0.89 ± 0.05 | 1.02 ± 0.10 | 0.89 ± 0.15 | 0.88 ± 0.08 | 0.87 ± 0.06 | 0.88 ± 0.09 | 1.01 ± 0.08 |
| | 40 | 0.94 ± 0.06 | 0.92 ± 0.05 | 1.04 ± 0.09 | 0.93 ± 0.15 | 0.88 ± 0.06 | 0.89 ± 0.08 | 0.90 ± 0.07 | 1.02 ± 0.06 |
| | 60 | 1.00 ± 0.07 | 0.93 ± 0.06 | 1.06 ± 0.09 | 1.02 ± 0.14 | 0.90 ± 0.06 | 0.90 ± 0.09 | 0.94 ± 0.08 | 1.05 ± 0.04 |
| | 80 | 1.07 ± 0.09 | 0.94 ± 0.06 | 1.11 ± 0.18 | 1.07 ± 0.14 | 0.92 ± 0.08 | 0.91 ± 0.07 | 0.95 ± 0.09 | 1.09 ± 0.05 |

**Table 8**
Coefficient of joint variation on T2-w axial images of BrainWeb dataset.

| Noise level (%) | Bias field (%) | Original | N4 | LSACM | MICO | IACM | Proposed | NIMS | MFCM |
|---|---|---|---|---|---|---|---|---|---|
| 1 | 20 | 0.71 ± 0.05 | 0.69 ± 0.05 | 0.75 ± 0.35 | 0.70 ± 0.04 | 0.70 ± 0.02 | 0.70 ± 0.03 | 0.69 ± 0.07 | 0.72 ± 0.16 |
| | 40 | 0.75 ± 0.06 | 0.70 ± 0.05 | 0.76 ± 0.19 | 0.72 ± 0.04 | 0.74 ± 0.04 | 0.70 ± 0.06 | 0.70 ± 0.07 | 0.75 ± 0.09 |
| | 60 | 0.80 ± 0.07 | 0.72 ± 0.06 | 0.86 ± 0.21 | 0.71 ± 0.04 | 0.74 ± 0.07 | 0.72 ± 0.04 | 0.73 ± 0.07 | 0.87 ± 0.14 |
| | 80 | 0.86 ± 0.08 | 0.76 ± 0.07 | 0.89 ± 0.24 | 0.71 ± 0.05 | 0.73 ± 0.08 | 0.72 ± 0.06 | 0.74 ± 0.06 | 0.88 ± 0.04 |
| 5 | 20 | 1.06 ± 0.06 | 1.04 ± 0.05 | 1.13 ± 0.20 | 1.03 ± 0.06 | 1.02 ± 0.09 | 1.02 ± 0.05 | 1.04 ± 0.09 | 1.15 ± 0.18 |
| | 40 | 1.10 ± 0.06 | 1.05 ± 0.05 | 1.16 ± 0.11 | 1.03 ± 0.06 | 1.01 ± 0.05 | 1.02 ± 0.08 | 1.04 ± 0.08 | 1.15 ± 0.16 |
| | 60 | 1.15 ± 0.07 | 1.08 ± 0.06 | 1.19 ± 0.10 | 1.03 ± 0.06 | 1.02 ± 0.07 | 1.04 ± 0.04 | 1.06 ± 0.08 | 1.21 ± 0.09 |
| | 80 | 1.20 ± 0.09 | 1.12 ± 0.06 | 1.24 ± 0.09 | 1.03 ± 0.05 | 1.02 ± 0.10 | 1.06 ± 0.07 | 1.10 ± 0.08 | 1.23 ± 0.15 |
| 9 | 20 | 1.58 ± 0.09 | 1.55 ± 0.08 | 1.67 ± 0.22 | 1.49 ± 0.10 | 1.47 ± 0.13 | 1.46 ± 0.09 | 1.54 ± 0.16 | 1.68 ± 0.12 |
| | 40 | 1.63 ± 0.10 | 1.57 ± 0.08 | 1.70 ± 0.16 | 1.49 ± 0.10 | 1.48 ± 0.15 | 1.47 ± 0.15 | 1.55 ± 0.11 | 1.69 ± 0.17 |
| | 60 | 1.68 ± 0.11 | 1.61 ± 0.08 | 1.77 ± 0.15 | 1.49 ± 0.09 | 1.48 ± 0.15 | 1.50 ± 0.14 | 1.62 ± 0.12 | 1.79 ± 0.16 |
| | 80 | 1.74 ± 0.13 | 1.66 ± 0.09 | 1.80 ± 0.14 | 1.50 ± 0.08 | 1.48 ± 0.15 | 1.50 ± 0.07 | 1.63 ± 0.10 | 1.81 ± 0.09 |

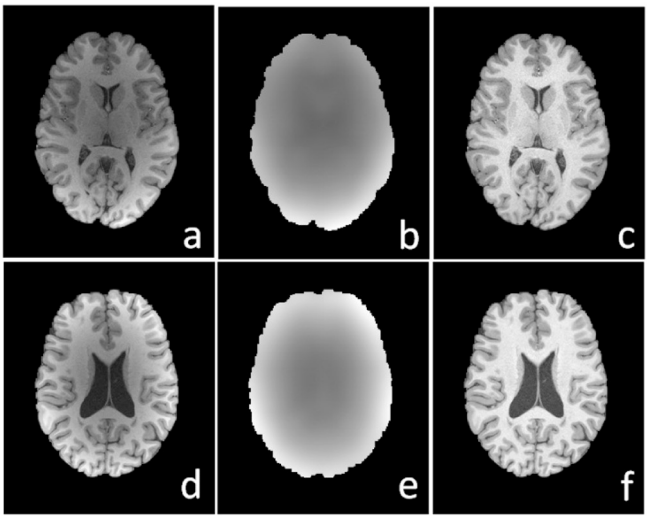


**Fig. 4.** Intensity inhomogeneity correction on real T1-w images. [a, d] T1-w axial original images of two randomly chosen patients, [b, e] Estimated bias field in [a] and [d], [c, f] Corrected images of [a] and [d].

5 iterations of the AM scheme. The processing times on different modalities were found to be almost similar when implemented with same values for parameters. It was also noted that the average processing time remained almost constant irrespective of the inhomogeneity level in the input image.

### 3.2. HCP dataset

A detailed validation of the proposed methodology was carried out on real brain MR images of the HCP dataset[2] [82]. The dataset contains T1-w and T2-w structural MR images of healthy adults from a Siemens Skyra 3T scanner. Scanning protocol details are provided in [83].

The results obtained after application of the proposed methodology on real T1-w images are shown in Fig. 4. Fig. 4.a and Fig. 4.d are T1-w mid-slices of two randomly chosen patient's data and the second column shows the estimated bias field and corrected images after the application of the proposed methodology is provided in the third column. The images in the database were free from noises. From Fig. 4, it is observed that intensities in various tissue regions of the corrected images appear more identical compared to that of the original images. This is clearly evident in the white matter regions of the T1-w image provided in Fig. 4.c and Fig. 4.f.

Fig. 5 shows the results obtained on T2-w axial images of two different randomly chosen patients' data provided in Fig. 4. It is observed from Fig. 5 that the bias field estimated was found to be smooth and the contrast between white matter and grey matter regions was improved after the correction. Thus the efficacy of the proposed method for intensity inhomogeneity correction in real data is verified visually. This has been confirmed again by comparing the intensity profile plots of the original data and the corrected data which is given in Fig. 6. It is

**Table 9**
Coefficient of joint variation on PD axial images of BrainWeb dataset.

| Noise level (%) | Bias field (%) | Original | N4 | LSACM | MICO | IACM | Proposed | NIMS | MFCM |
|---|---|---|---|---|---|---|---|---|---|
| 1 | 20 | 0.58 ± 0.07 | 0.44 ± 0.03 | 0.59 ± 0.12 | 0.51 ± 0.10 | 0.45 ± 0.04 | 0.43 ± 0.05 | 0.44 ± 0.04 | 0.61 ± 0.15 |
| | 40 | 0.88 ± 0.14 | 0.45 ± 0.02 | 0.69 ± 0.05 | 0.52 ± 0.09 | 0.46 ± 0.05 | 0.44 ± 0.08 | 0.44 ± 0.06 | 0.80 ± 0.12 |
| | 60 | 1.22 ± 0.24 | 0.45 ± 0.07 | 0.71 ± 0.05 | 0.52 ± 0.10 | 0.46 ± 0.04 | 0.45 ± 0.04 | 0.45 ± 0.08 | 0.71 ± 0.17 |
| | 80 | 1.58 ± 0.38 | 0.46 ± 0.05 | 0.71 ± 0.14 | 0.53 ± 0.08 | 0.48 ± 0.08 | 0.45 ± 0.09 | 0.47 ± 0.05 | 0.72 ± 0.12 |
| 5 | 20 | 1.06 ± 0.09 | 0.95 ± 0.06 | 1.08 ± 0.09 | 0.94 ± 0.09 | 0.98 ± 0.08 | 0.92 ± 0.08 | 0.94 ± 0.07 | 1.00 ± 0.15 |
| | 40 | 1.29 ± 0.16 | 0.97 ± 0.08 | 1.25 ± 0.07 | 0.95 ± 0.07 | 0.99 ± 0.05 | 0.93 ± 0.11 | 0.96 ± 0.10 | 1.06 ± 0.09 |
| | 60 | 1.58 ± 0.27 | 0.96 ± 0.08 | 1.54 ± 0.08 | 0.95 ± 0.08 | 1.01 ± 0.07 | 0.94 ± 0.13 | 1.00 ± 0.04 | 1.08 ± 0.14 |
| | 80 | 1.91 ± 0.42 | 0.97 ± 0.10 | 1.58 ± 0.19 | 0.94 ± 0.09 | 1.00 ± 0.10 | 0.94 ± 0.15 | 1.01 ± 0.08 | 1.35 ± 0.19 |
| 9 | 20 | 1.73 ± 0.15 | 1.53 ± 0.14 | 1.75 ± 0.16 | 1.58 ± 0.12 | 1.51 ± 0.12 | 1.50 ± 0.09 | 1.52 ± 0.12 | 1.55 ± 0.09 |
| | 40 | 1.94 ± 0.24 | 1.54 ± 0.13 | 1.90 ± 0.19 | 1.61 ± 0.10 | 1.54 ± 0.12 | 1.51 ± 0.11 | 1.52 ± 0.14 | 1.58 ± 0.17 |
| | 60 | 2.20 ± 0.37 | 1.54 ± 0.12 | 2.01 ± 0.17 | 1.60 ± 0.14 | 1.55 ± 0.13 | 1.52 ± 0.12 | 1.53 ± 0.15 | 1.58 ± 0.21 |
| | 80 | 2.51 ± 0.57 | 1.54 ± 0.11 | 2.51 ± 0.26 | 1.62 ± 0.12 | 1.58 ± 0.09 | 1.53 ± 0.14 | 1.56 ± 0.13 | 1.97 ± 0.26 |

CV values in white matter and grey matter regions. This observation might be taken as an indirect evidence of the ineffective smoothing strategy adopted for the estimated bias field [81]. The quantitative results from Tables 1–6 pronounce the robustness of the proposed methodology to noise. The proposed methodology provided the least CJV in higher simulated noise levels. The results verify the property of $L_1$ norm minimization of the framelet coefficients to suppress noise. The sparse approximation of the corrected image in the framelet domain not only helps to preserve the multiscale edges but also offers robustness to noise. In this experiment, the algorithm was converged in an average of

[2] http://www.humanconnectome.org

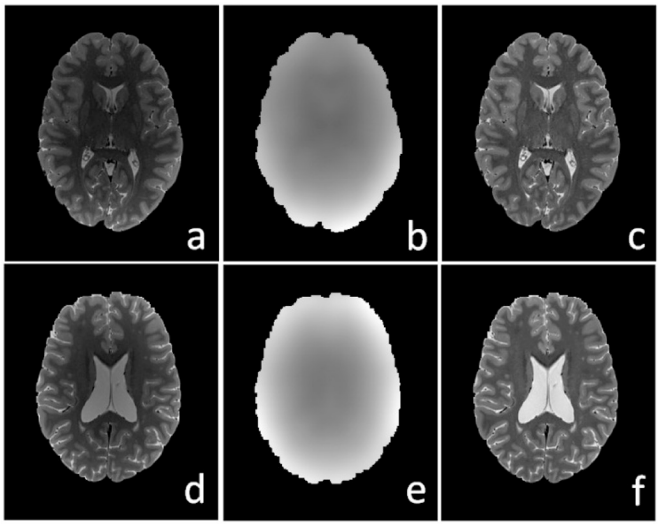


**Fig. 5.** Intensity inhomogeneity correction on real T2-w images. [a, d] T2-w axial original images of two randomly chosen patients, [b, e] Estimated bias field in [a] and [d], [c, f] Corrected images of [a] and [d].

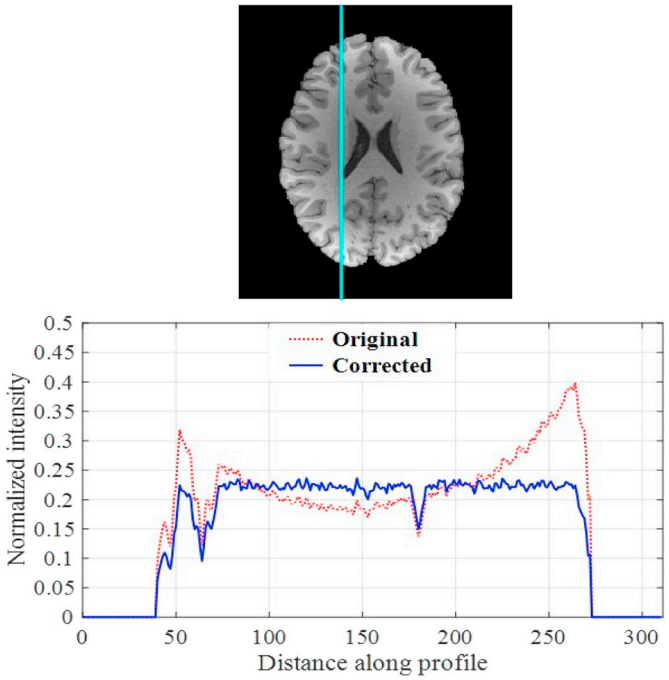


**Fig. 6.** Comparison of intensity profiles. Intensity profile plots of the original data (red) and the corrected data (blue) along the selected line shown in the T1-w axial image. (For interpretation of the references to color in this figure legend, the reader is referred to the web version of this article.)

observed that the variations in the white matter region before correction have been significantly reduced after the application of the proposed methodology. It is also worth to note that the sudden variations indicating the edges in the profile plot are preserved which could be attributed to the sparsity constraint imposed in the framelet domain.

The CV values were calculated before and after the application of the proposed methodology in order to evaluate the reduction in the intra-class variations in white matter and grey matter tissue regions. Table 10 shows the average CV values of the 30 selected image volumes. The corresponding box-whisker plot of the CV values is shown in Fig. 7.

It is evident from Table 10 that there is an obvious reduction in the average CV values after the application of all the seven algorithms under consideration. And the proposed methodology has shown superior performance in the correction in terms of CV values. The correction of high intensity variations visible in white matter tissue regions in T1-w image by visual analysis has been effectively justified quantitatively through the reduction of CV values in white matter. The average CJV values between white matter and grey matter are also tabulated in Table 11 and the same is depicted in box-whisker plot in Fig. 8. It is clearly evident that the performance of proposed methodology is found to be satisfactory and is better than other seven algorithms considered in terms of both CV and CJV values. The AM algorithm took an average of 4 AM iterations in the HCP dataset.

During the implementation of the proposed algorithm on both datasets, $\mu^0$ and ρ were taken to be 3 and 2 empirically. The value of $\alpha$ was considered to be $\|\mathscr{F}(r)\|_1/\|\mathscr{F}(b^0)\|_1$ where $r$ is the input image and $b^0$ is the initial estimate of the bias field. The initial estimate $b^0$ is a Gaussian low-pass version of the input image. A higher $\alpha$ value delivers a greater degree of sparsity to the bias field in Fourier domain which in turn improves the degree of smoothness. The iterations were stopped if normalized mean square errors $\frac{\|b^{k+1}-b^k\|}{\|b^{k+1}\|}$ and $\frac{\|s^{k+1}-s^k\|}{\|s^{k+1}\|}$ fall below chosen thresholds, $\omega_b$ and $\omega_s$ respectively. Both the thresholds were chosen to be $10^{-3}$ for simulated and real datasets. This stopping criterion was selected empirically by observing the satisfactory reduction in CV and CJV values with respect to the ground truth image in simulated database. The proposed algorithm requires only four predefined parameters that are $\mu^0$, ρ, $\omega_b$ and $\omega_s$. The number of user-defined parameters is significantly fewer and they don't critically control the correction unlike the other algorithms considered. However, the proposed algorithm is designed for inhomogeneity correction in 2D images and therefore volume data will be processed only in slice-by-slice manner. Further, framelet transform computations contribute to an increased computational complexity. The computational complexity of the algorithm increases with the size of the input image and rescaling the input image may reduce the accuracy of the correction.

## 4. Conclusion

An effective retrospective correction method for intensity inhomogeneity in MR images is proposed in this paper.

**Table 10**
Coefficient of variation on HCP real dataset.

| | | Input | Bias field corrected data | | | | | | |
|---|---|---|---|---|---|---|---|---|---|
| | | | N4 | LSACM | MICO | IACM | Proposed | NIMS | MFCM |
| T1-w | GM | 28.54 ± 4.20 | 19.77 ± 2.88 | 14.38 ± 1.02 | 12.25 ± 0.62 | 15.48 ± 1.30 | 12.08 ± 0.82 | 13.67 ± 1.14 | 20.65 ± 1.45 |
| | WM | 24.26 ± 3.67 | 12.51 ± 2.59 | 8.96 ± 1.41 | 8.87 ± 1.98 | 11.60 ± 1.31 | 8.05 ± 0.73 | 9.50 ± 1.14 | 16.26 ± 2.75 |
| T2-w | GM | 30.97 ± 3.64 | 21.21 ± 3.40 | 20.57 ± 2.19 | 20.46 ± 2.45 | 21.77 ± 2.46 | 15.75 ± 1.49 | 17.66 ± 2.26 | 25.27 ± 3.29 |
| | WM | 33.65 ± 5.00 | 27.40 ± 4.52 | 19.92 ± 2.82 | 22.48 ± 3.11 | 22.20 ± 2.49 | 18.34 ± 2.93 | 20.04 ± 2.70 | 30.37 ± 3.82 |

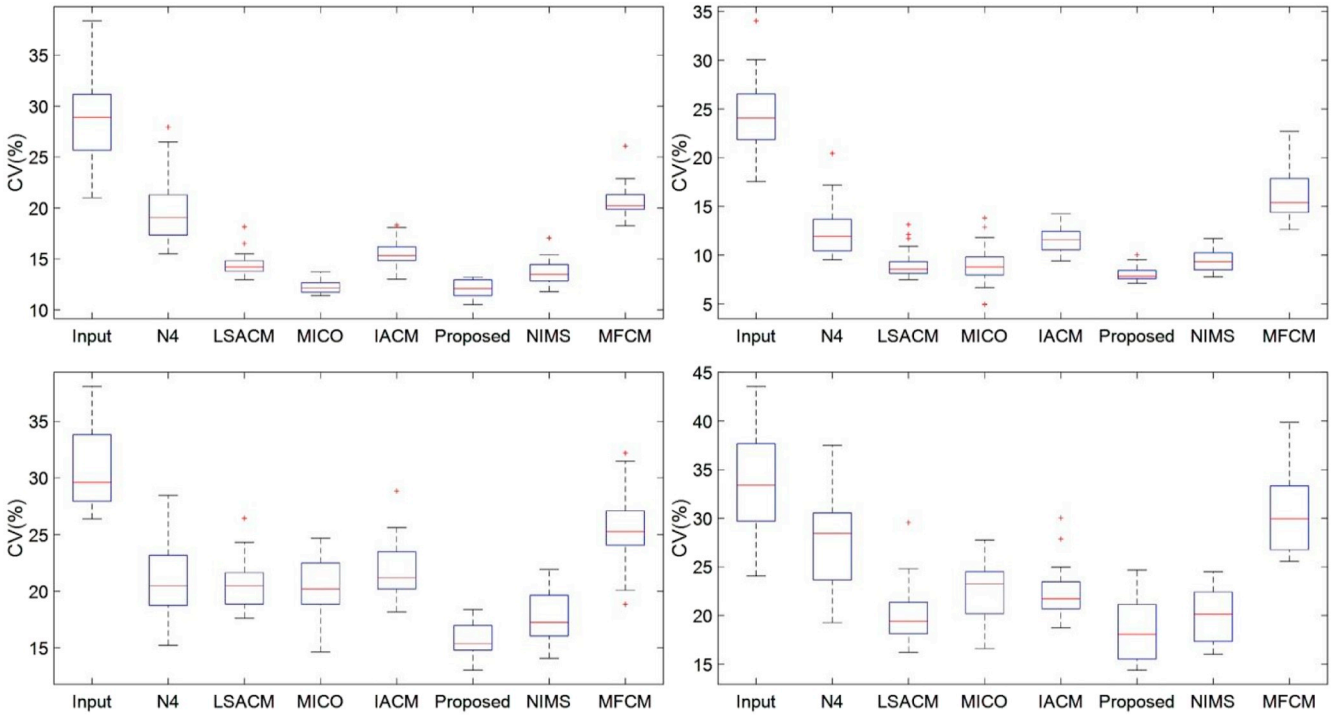


**Fig. 7.** Box-whisker plot of average CV. Row 1: CV in percentage for grey matter (left) and white matter (right) in T1-w images, Row 2: CV in percentage for grey matter (left) and white matter (right) in T2-w images.

**Table 11**
Coefficient of joint variation on HCP real dataset.

| | Input | Bias field corrected data | | | | | | |
|---|---|---|---|---|---|---|---|---|
| | | N4 | LSACM | MICO | IACM | Proposed | NIMS | MFCM |
| T1-w | 2.84 ± 0.57 | 1.61 ± 0.30 | 1.22 ± 0.28 | 0.98 ± 0.08 | 1.21 ± 0.14 | 0.80 ± 0.11 | 0.91 ± 0.14 | 1.94 ± 0.28 |
| T2-w | 1.41 ± 0.22 | 1.27 ± 0.18 | 1.07 ± 0.14 | 1.16 ± 0.12 | 1.02 ± 0.11 | 1.03 ± 0.10 | 1.17 ± 0.10 | 1.33 ± 0.18 |

The proposed methodology was evolved from a primitive energy minimization model for intensity inhomogeneity correction. In the proposed methodology, the primitive model is suitably modified to accomplish effective intensity inhomogeneity correction by considering sparsity constraints in appropriate transform domains. Intensity inhomogeneity problem is formulated in an optimization framework that seeks decomposition of the acquired image into a piecewise constant corrected image and a smooth bias field with sparsity constraints. The sparsity constraints are imposed based on the known spatial properties of bias field and true image. The sparse representation under a tight framelet system realized with $L_1$ norm minimization can effectively impose piecewise constant nature in the corrected image while preserving the multi-scale edges. Further, the spatial smoothness of the bias field ensures a sparse representation in the Fourier domain and hence $L_1$ norm minimization of the Fourier coefficients enforces to obtain slowly varying bias field.

The corrected image is assumed to have a sparse representation in the framelet domain as it imposes piecewise constant nature while preserving the multi-scale edges. The bias field is known to be spatially smooth and therefore is expected to be sparse in the Fourier domain. In the proposed methodology, the optimal sparse solutions for corrected image and bias field in the suitable transformed domain are realized by $L_1$ norm minimization. The proposed constrained optimization problem which is convex is efficiently solved by the linearized augmented Lagrangian method. Thus ill-posed problem of intensity inhomogeneity correction is solved effectively with only sparsity constraints avoiding the need for any predefined specifications or parametric models that are critically controlled by user-defined parameters.

The performance of the proposed algorithm was evaluated quantitatively on simulated BrainWeb dataset through CV in white matter and grey matter regions in T1-w, T2-w and PD modalities. The results validate the reduced intra-class variations in the intensity levels observed in the qualitative analysis. A considerable reduction in CJV values was also noticed irrespective of the image modality and the inhomogeneity level. It is observed from the quantitative validation on the simulated dataset that the proposed algorithm offered better performance in terms of CV and CJV values when compared with some of the distinguished algorithms for intensity inhomogeneity correction. The proposed methodology maintains consistency in the performance irrespective of the noise level unlike the some of the other methods considered. The sparisty constraint imposed in framelet domain to enforce the piecewise constant nature inherits to suppress noise while preserving multi-scale edges. This justifies the consistent performance at higher noise levels as observed during the experimental analysis.

The proposed algorithm delivered a satisfactory correction for intensity inhomogeneity in real human brain MR dataset. The quantitative results in terms of CV and CJV prove that inter-class separation is improved and intra-class intensity variations are also reduced after the

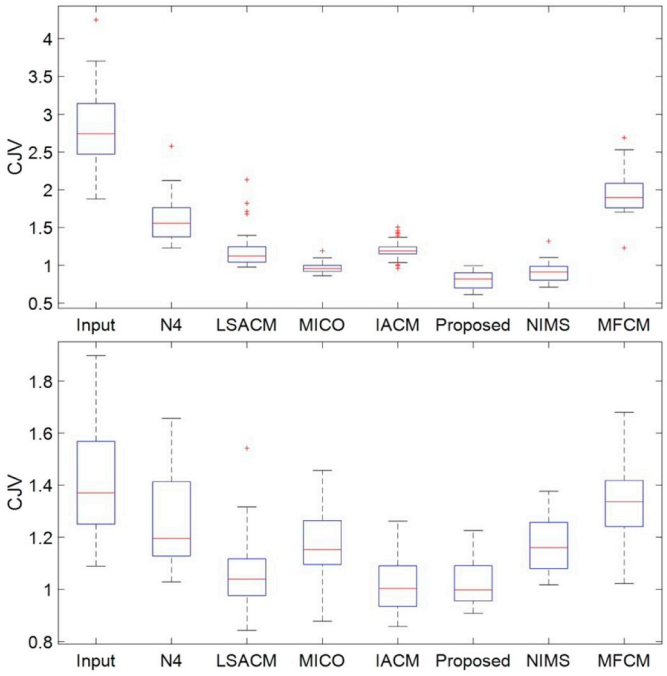


**Fig. 8.** Box Whisker plot of average CJV. Row 1: CJV between white matter and grey matter in T1-w images. Row 2: CJV between white matter and grey matter in T2-w images.

correction. The proposed algorithm produced the lowest CV and CJV values during the performance comparison with other algorithms in both T1-w and T2-w modalities. It is worth to note from the intensity profile analysis of the corrected image in real data that the framelet norm constraint has helped to obtain a piecewise constant image without diminishing the edges in the image. And the smoothness has been achieved without assuming any parametric model to the bias field that required critical parameters to be defined. The methodology requires less number of user defined parameters and the impact of the parameters on the accuracy of intensity correction is significantly reduced compared to the other distinguished algorithms considered.

## Funding

No specific grant was received for this research from funding agencies in the public, commercial, or not-for-profit sectors.

## Conflict of interests

The authors of this paper do not have any conflicts of interest to report.

## Acknowledgement

Real data used in results section were provided by the Human Connectome Project, WU-Minn Consortium (Principal Investigators: David Van Essen and Kamil Ugurbil; 1U54MH091657) funded by the 16 NIH Institutes and Centers that support the NIH Blueprint for Neuroscience Research; and by the McDonnell Center for Systems Neuroscience at Washington University.

The authors are grateful to Dr. Devakumar Devadhas, Christian Medical College, Vellore, India for the clinical validation of the proposed methodology and valuable suggestions provided.

## Appendix A. Tight framelet system

Images have sparse approximations under certain tight frame systems such as curvelets, framelets, Gabor transform, translation invariant wavelets etc. Sparsity under suitable tight frame systems have been utilized in various image restoration applications [84–86]. Tight frames form redundant orthogonal bases in $\mathbb{R}^n$. The redundant nature of the tight frame facilitates robustness againt noise and partial loss of data. Let the analysis and synthesis operators of a tight frame be $D$ and $D^T$ and they must satisfy the criteria $D^TD = I$.

A countable set $X \subset L^2(\mathbb{R})$ is a tight frame if

$$f = \sum_{\Phi \in X} \langle f, \Phi \rangle \Phi \; \forall \, f \in L^2(\mathbb{R}) \tag{A.1}$$

where, $\langle \cdot, \cdot \rangle$ is the inner product of $L^2(\mathbb{R})$. For a finite set of generating functions, $\Psi := \{\psi_1, \psi_2, \ldots, \psi_n\} \subset L^2(\mathbb{R})$, the wavelet system defined by dilations and shifts as follows;

$$X(\Psi) := \{2^{j/2}\, \psi_l\, (2^j \bullet - k)\; 1 \le l \le n; j, k \in \mathbb{Z}\} \tag{A.2}$$

$X(\Psi)$ is called a tight wavelet frame if it forms a tight frame of $L^2(\mathbb{R})$ and each $\psi_l$ is called a framelet.

A set of framelets can be constructed from a compactly supported refinable function $\phi$ which is a scaling function and refinement mask $\tau_\phi$ satisfying,

$$\widehat{\phi}\,(2\omega) = \tau_\phi \widehat{\phi}\,(\omega) \tag{A.3}$$

where, $\widehat{\phi}$ represents the Fourier transform of $\phi$ and $\tau_\phi$ is a polynomial satisfying $\tau_\phi(0) = 1$ which implies it to be a lowpass filter. If a refinable function $\widehat{\phi}$ is known, then the finite set $\Psi$ in Fourier domain that forms the tight framelet system satisfies the following for some $2\pi$-periodic $\tau_\psi$.

$$\widehat{\psi}\,(2\omega) = \tau_\psi \widehat{\phi}\,(\omega) \tag{A.4}$$

By unitary extension principle, the following criteria also has to be satisfied to construct tight wavelet frame,

$$\tau_\phi(\omega)\overline{\tau_\phi(\omega + \gamma\pi)} + \sum_l \tau_{\psi_l}\overline{\tau_{\psi_l}(\omega + \gamma\pi)} = \delta(\gamma)\, \gamma = 0, 1 \tag{A.5}$$

The above equation insists $\{\tau_{\psi_l}\}$ to be a high pass filter. In a framelet system, an image can be considered as the coefficients obtained $\{y_i = \langle y, \Phi(\cdot - \mathrm{i})\rangle^{j/2}\}$. The framelet decomposition of the image at a level $L$ consists of the coefficients, $\{\langle y, 2^{L/2}\, \Phi(2^L \cdot - \mathrm{j})\rangle\}$. Therefore, the $L-$level decompisition of the image will have the coefficients, $\{\langle y, 2^{l/2}\, \psi_i(2^l \cdot - \mathrm{j})\rangle, 1 \le i \le n^2 - 1\}$ for $1 \le l \le L$. This composition can be realized into a linear operator $W \in \mathbb{R}^{k \times n}$ satisying $W^TW = I$ and the row vactors of the analysis operator form a tight frame system in $\mathbb{R}^n$. The derivation of $W$ from the filters associated a framelet is provided below.

Considere a vector $a = [a_0, a_1, a_2, \ldots. a_N]$ of length $N$. Here, $W$ which is a Toeplitz-Hankel matrix is derived assuming the Neumann boundary

conditions. Let there be $K$ filters associated with the framelet system denoted by $\{h_i\}_{i=0}^{K-1}$. The analysis operator $W$ is formed from a set of Toeplitz-Hankel matrices of the associated filters denoted by $\{Q_i\}_{i=0}^{K-1}$. Where, $Q_i$ = Toeplitz − Hankel ($h_i$).

The Toeplitz-Hankel matrix for a filter $g = [g_{-N}, g_{-N+1}, \ldots g_0, \ldots, g_{N-1}, g_N]$ is defined by,

$$\text{Toeplitz}-\text{Hankel}\,(g) = Hankel\,(g_l) + Toeplitz\,(g) + Hankel\,(g_r)$$

$$Hankel\,(g_l) = \begin{bmatrix} g_1 & \cdots & g_N \\ \vdots & \iddots & \\ g_N & & 0 \end{bmatrix}$$

$$Hankel\,(g_r) = \begin{bmatrix} 0 & & g_{-N} \\ & \iddots & \vdots \\ g_{-N} & \cdots & g_{-1} \end{bmatrix}$$

$$Toeplitz\,(g) = \begin{bmatrix} g_0 & g_{-1} & \cdots & g_{-N+2} & g_{-N+1} \\ g_1 & g_0 & \cdots & g_{-N+3} & g_{-N+2} \\ \vdots & \vdots & \ddots & \vdots & \vdots \\ g_{N-2} & g_{N-3} & \cdots & g_0 & g_{-1} \\ g_{N-1} & g_{N-2} & \cdots & g_1 & g_0 \end{bmatrix} \tag{A.6}$$

Therefore, for the vector $a$ under the perfect reconstrunction of the framelet transform,

$$a = \sum_i Q_i^* Q_i a \tag{A.7}$$

A piecewise linear B-spline framelet formation is provided in [69] for which the refinement mask $\tau_\phi(\omega) = cos^2\left(\frac{\omega}{2}\right)$. The lowpass filter corresponding to this refinement mask is $h_0 = \frac{1}{4}[1, 2, 1]$.And the framelets $\tau_{\psi_1} = -\frac{\sqrt{2}i}{2} sin\,(\omega)$ and $\tau_{\psi_2} = sin^2\left(\frac{\omega}{2}\right)$ are highpass filters given as $h_1 = \frac{\sqrt{2}}{4}[1, 0, -1]$ and $h_2 = \frac{1}{4}[-1, 2, -1]$.The analysis opertor $W$ of this framelet system can be obtained from $h_0$, $h_1$, $h_2$ by procedure descibed above.

## Appendix B

The performance of the proposed method was compared with some of the recent retrospective methods. This section lists the parameters utilized for all the other algorithms considered in the performance comparison. For a fair comparison, the methods requiring contour initialization have been set using K-means algorithm

N4

The N4 bias field corrections were performed in the 3DSlicer software (https://www.slicer.org) which has an integrated N4ITK MRI Bias correction module. The default parameters of N4 in the slicer software were utilized for corrections in simulated and real brain datasets. The following screenshot shows the defaults parameters for N4 in the Slicer software followed by detailed description of the default values.

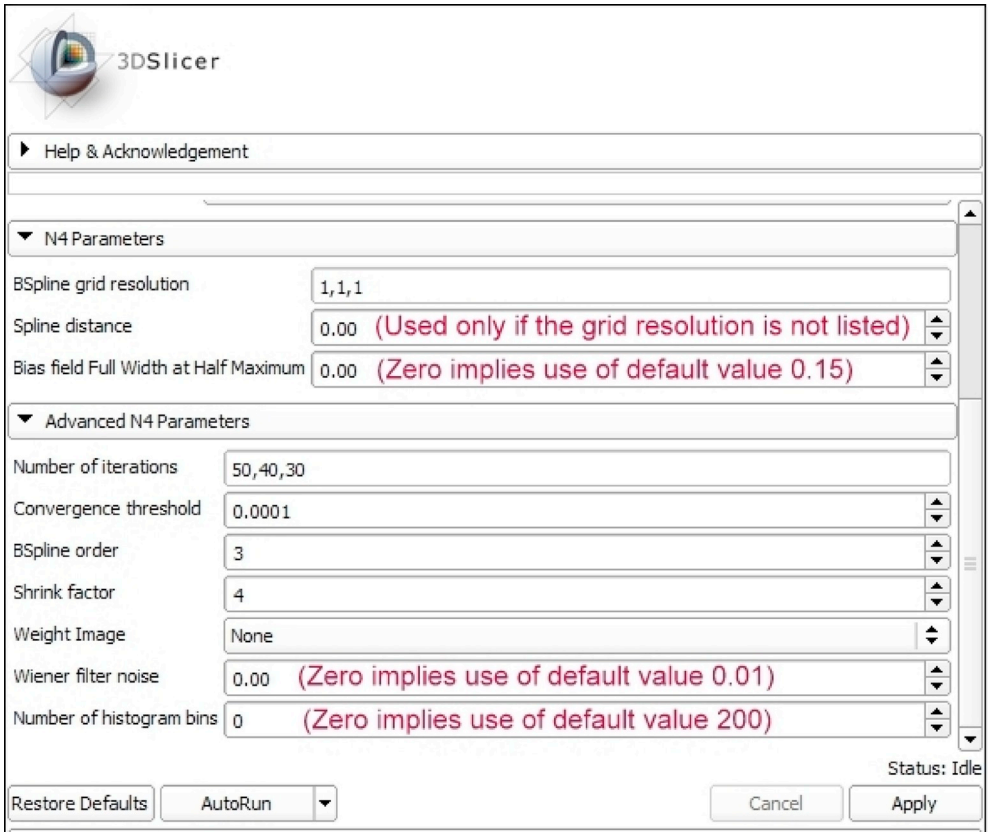


**Fig. B1.** N4ITK panel with default parameters in the 3D slicer software.

The spline distance is used only when the grid resolution is not specified. The value of Bias field Full Width at Half Maximum, Wiener filter noise and Number of histogram bins are set to zero to imply the use of default values which are 0.15, 0.01 and 200 respectively.

**N4 default parameters in slicer software**:

- **BSpline grid resolution**: This parameter is a sequence of three numbers that specify the initial bspline grid resolution. The actual resolution will be defined by adding the bspline order (3) to the resolution which results in a 4 × 4 × 4 grid of control points here.
- **Spline distance**: This parameter refers to the distance between the control points and is used only if the grid resolution is not listed.
- **Bias field Full Width at Half Maximum**: This parameter is set as zero to imply use of the default value (0.15).

- **Advanced N4 Parameters**:
  - **Number of iterations**: Maximum number of iterations at each level of resolution.
  - **Convergence threshold**: The stopping criterion for the iterative algorithm.
  - **BSpline order**: Order of B-spline used in the approximation.
  - **Shrink factor**: Defines how much the image should be upsampled before estimating the inhomogeneity field.
  - **Weight Image**: Weight Image
  - **Wiener filter noise**: Wiener filter noise. Zero implies use of the default value.
  - **Number of histogram bins**: Number of histogram bins. Zero implies use of the default value.

Slicer code for N4ITK with detailed description is available at https://framagit.org/OpenAtWork/Slicer/blob/465f34f241ca219b24080a8b84ef10a7587264ef/Applications/CLI/N4ITKBiasFieldCorrection/N4ITKBiasFieldCorrection.xml

The default parameters were utilized for the other six algorithms which are listed below;

| Method | Parameters and values |
|---|---|
| LSACM | Time step for level set evolution $\Delta t$<br>Time step for regularization $\Delta t_1 = 1$<br>$\varepsilon = 1$<br>Region scale parameter $\rho = 6$<br>Maximum number of iterations = 15 |
| MICO | M = 20<br>$\varepsilon = 0.001$<br>$N = 3$<br>q = 1 |
| NIMS | $\lambda_1 = \frac{(M+N)}{16}$ where M,N are the input image dimensions<br>$\delta = 3$<br>$k_\beta = 0.55$<br>$M_b, N_b = \frac{\mathrm{Max}\,(M,N)}{4}$ |
| MFCM | $\alpha = 0.7$<br>$p = 2$<br>$N_R = 9$ (3 × 3 window)<br>$\varepsilon = 0.01$ |
| Proposed | $\mu^0 = 3$<br>$\rho = 2$<br>$\omega_b = 10^{-3}$<br>$\omega_s = 10^{-3}$ |
| IACM | $\varepsilon = 0.001$<br>$\beta = 0.02$<br>$m = 4$<br>$L = 15$<br>$\gamma = 1$<br>$\nu = 100$<br>Patch size = 3 × 3 |

## References


[1] Guillemaud R, Brady M. Estimating the bias field of MR images. IEEE Trans Med Imaging 1997;16:238–51. https://doi.org/10.1109/42.585758.

[2] Shattuck DW, Sandor-Leahy SR, Schaper KA, Rottenberg DA, Leahy RM. Magnetic resonance image tissue classification using a partial volume model. Neuroimage 2001;13:856–76. https://doi.org/10.1006/nimg.2000.0730.

[3] Worth AJ, Makris N, Caviness Jr. VS, Kennedy DN. Neuroanatomical segmentation in MRI: technological objectives. Int J Pattern Recognit Artif Intell 1997;11:1161–87. https://doi.org/10.1142/S0218001497000548.

[4] Ling Q, Li Z, Huang Q, Li X. A Robust gradient-based algorithm to correct Bias fields of brain MR images. IEEE Trans Auton Ment Dev 2015;7:256–64. https://doi.org/10.1109/TAMD.2015.2416976.

[5] Simmons A, Tofts PS, Barker GJ, Arridge SR. Sources of intensity nonuniformity in spin echo images at 1.5 T. Magn Reson Med 1994;32:121–8. https://doi.org/10.1002/mrm.1910320117.

[6] Liang Z-P, Lauterbur PC, IEEE Engineering in Medicine and Biology Society. Principles of magnetic resonance imaging: a signal processing perspective. SPIE Optical Engineering Press; 2000.

[7] Keiper MD, Grossman RI, Hirsch JA, Bolinger L, Ott IL, Mannon LJ, et al. MR identification of white matter abnormalities in multiple sclerosis: a comparison between 1.5 T and 4 T. AJNR Am J Neuroradiol 1998;19:1489–93.

[8] Alecci M, Collins CM, Smith MB, Jezzard P. Radio frequency magnetic field mapping of a 3 Tesla birdcage coil: experimental and theoretical dependence on sample properties. Magn Reson Med 2001;46:379–85. https://doi.org/10.1002/mrm.1201.

[9] Materka Andrzej, Strzelecki M. On the importance of MRI nonuniformity correction for texture analysis. 2013 signal process. algorithms, archit. arrange. appl. 2013. p. 118–23.

[10] Vovk U, Pernus F, Likar B. A review of methods for correction of intensity inhomogeneity in MRI. IEEE Trans Med Imaging 2007;26:405–21. https://doi.org/10.1109/TMI.2006.891486.

[11] Zhou LQ, Zhu YM, Bergot C, Laval-Jeantet AM, Bousson V, Laredo JD, et al. A method of radio-frequency inhomogeneity correction for brain tissue segmentation in MRI. Comput Med Imaging Graph 2001;25:379–89.

[12] Narayana PA, Borthakur A. Effect of radio frequency inhomogeneity correction on the reproducibility of intra-cranial volumes using MR image data. Magn Reson Med 1995;33:396–400.

[13] George MM, Kalaivani S, Sudhakar MS. A non-iterative multi-scale approach for intensity inhomogeneity correction in MRI. Magn Reson Imaging 2017;42:43–59. https://doi.org/10.1016/j.mri.2017.05.005.
[14] Wells WM, Grimson WEL, Kikinis R, Jolesz FA. Adaptive segmentation of MRI data. IEEE Trans Med Imaging 1996;15:429–42. https://doi.org/10.1109/42.511747.
[15] Gispert JD, Reig S, Pascau J, Vaquero JJ, García-Barreno P, Desco M. Method for bias field correction of brain T1-weighted magnetic resonance images minimizing segmentation error. Hum Brain Mapp 2004;22:133–44. https://doi.org/10.1002/hbm.20013.
[16] Andersen AH, Zhang Z, Avison MJ, Gash DM. Automated segmentation of multispectral brain MR images. J Neurosci Methods 2002;122:13–23. https://doi.org/10.1016/S0165-0270(02)00273-X.
[17] Ahmed MN, Yamany SM, Farag AA, Moriarty T. Bias field estimation and adaptive segmentation of MRI data using a modified fuzzy C-means algorithm. Proceedings. 1999 IEEE comput. soc. conf. comput. vis. pattern recognit. (Cat. No PR00149), IEEE comput. soc 1999. p. 250–5. https://doi.org/10.1109/CVPR.1999.786947.
[18] Pham DL, Prince JL. An adaptive fuzzy C-means algorithm for image segmentation in the presence of intensity inhomogeneities. Pattern Recogn Lett 1999;20:57–68. https://doi.org/10.1016/S0167-8655(98)00121-4.
[19] Ahmed MN, Yamany SM, Mohamed N, Farag AA, Moriarty T. A modified fuzzy c-means algorithm for bias field estimation and segmentation of MRI data. IEEE Trans Med Imaging 2002;21:193–9. https://doi.org/10.1109/42.996338.
[20] Derganc J, Likar B, Pernus F. Nonparametric segmentation of multispectral MR images incorporating spatial and intensity information. In: Sonka M, Fitzpatrick JM, editors. International society for optics and photonics vol. 4684. 2002. p. 391. https://doi.org/10.1117/12.467181.
[21] Likar B, Derganc J, Pernus F. Segmentation-based retrospective correction of intensity nonuniformity in multispectral MR images. In: Sonka M, Fitzpatrick JM, editors. Proc. SPIE 4684, med. imaging 2002 image process., vol. 4684, international society for optics and photonics 2002. p. 1531. https://doi.org/10.1117/12.467120.
[22] Li C, Gore JC, Davatzikos C. Multiplicative intrinsic component optimization (MICO) for MRI bias field estimation and tissue segmentation. Magn Reson Imaging 2014;32:913–23. https://doi.org/10.1016/j.mri.2014.03.010.
[23] Tustison NJ, Avants BB, Cook PA, Yuanjie Zheng Y, Egan A, Yushkevich PA, et al. N4ITK: improved N3 bias correction. IEEE Trans Med Imaging 2010;29:1310–20. https://doi.org/10.1109/TMI.2010.2046908.
[24] Lai S-H, Fang M. A new variational shape-from-orientation approach to correcting intensity inhomogeneities in magnetic resonance images. Med Image Anal 1999;3:409–24. https://doi.org/10.1016/S1361-8415(99)80033-4.
[25] Milles J, Zhu YM, Gimenez G, Guttmann CRG, Magnin IE. MRI intensity nonuniformity correction using simultaneously spatial and gray-level histogram information. Comput Med Imaging Graph 2007;31:81–90. https://doi.org/10.1016/J.COMPMEDIMAG.2006.11.001.
[26] Hernández JA, Mora ML, Schiavi E, Toharia P. RF inhomogeneity correction algorithm in magnetic resonance imaging. Berlin, Heidelberg: Springer; 2004. p. 1–8. https://doi.org/10.1007/978-3-540-30547-7_1.
[27] Chen Y, Xu Q, Zheng Y, Wang J, Kim J-U. Simultaneous intensity inhomogensity correction, registration and segmentation of anatomical structures from brain MR images. Int J Signal Process 2016;9:357–72. https://doi.org/10.14257/ijsip.2016.9.5.32.
[28] Chen Y, Wang Z, Jeon B, Wang J, Kim J-U. An automatical segmentation method for brain MR images. Adv Sci Tech 2016;123:171–7. https://doi.org/10.14257/astl.2016.123.33.
[29] Li C, Huang R, Ding Z. … JG-I transactions on, 2011 undefined. A level set method for image segmentation in the presence of intensity inhomogeneities with application to MRI. IEEE Trans Image Process 2011;20:2007–16.
[30] Zhang K, Zhang L, Lam K-M, Zhang D. A level set approach to image segmentation with intensity inhomogeneity. IEEE Trans Cybern 2016;46:546–57. https://doi.org/10.1109/TCYB.2015.2409119.
[31] Zhan T, Zhang J, Xiao L, Chen Y, Wei Z. An improved variational level set method for MR image segmentation and bias field correction. Magn Reson Imaging 2013;31:439–47. https://doi.org/10.1016/j.mri.2012.08.002.
[32] Ji Z, Xia Y, Sun Q, Cao G, Chen Q. Active contours driven by local likelihood image fitting energy for image segmentation. Inf Sci 2015;301:285–304. https://doi.org/10.1016/J.INS.2015.01.006.
[33] Tang J, Jiang XA. Variational level set approach based on local entropy for image segmentation and bias field correction. Comput Math Methods Med 2017;2017:9174275https://doi.org/10.1155/2017/9174275.
[34] Mumford D, Shah J. Optimal approximations by piecewise smooth functions and associated variational problems. Commun Pure Appl Math 1989;42:577–685. https://doi.org/10.1002/cpa.3160420503.
[35] Yuping Duan Y, Huibin Chang H, Weimin Huang W, Jiayin Zhou J, Zhongkang Lu Z, Chunlin Wu C. The L0 regularized Mumford–Shah model for bias correction and segmentation of medical images. IEEE Trans Image Process 2015;24:3927–38. https://doi.org/10.1109/TIP.2015.2451957.
[36] Chen Y, Zhao B, Zhang J, Zheng Y. Automatic segmentation for brain MR images via a convex optimized segmentation and bias field correction coupled model. Magn Reson Imaging 2014;32:941–55. https://doi.org/10.1016/j.mri.2014.05.003.
[37] Wenchao Cui, Guoqiang Gong, Ke Lu, Shuifa Sun, Fangmin D. Convex-relaxed active contour model based on localised kernel mapping. Institution of engineering and technology. vol. 11. 2007.
[38] Ben Salah M, Mitiche A, Ben Ayed I. Effective level set image segmentation with a kernel induced data term. IEEE Trans Image Process 2010;19:220–32. https://doi.org/10.1109/TIP.2009.2032940.
[39] Ben Salah M, Ben Ayed I, Yuan Jing, Zhang Hong. Convex-relaxed kernel mapping for image segmentation. IEEE Trans Image Process 2014;23:1143–53. https://doi.org/10.1109/TIP.2013.2297019.
[40] Ivanovska T, Laqua R, Wang L, Schenk A, Yoon JH, Hegenscheid K, et al. An efficient level set method for simultaneous intensity inhomogeneity correction and segmentation of MR images. Comput Med Imaging Graph 2016;48:9–20. https://doi.org/10.1016/j.compmedimag.2015.11.005.
[41] Yang Y, Li C, Kao C. Visual SO-IS on, 2010 undefined. Split Bregman method for minimization of region-scalable fitting energy for image segmentation. Int. Symp. Vis. Comput. Berlin, Heidelberg: Springer; 2010. p. 117–28.
[42] Yang Y, Zhao Y, Wu B, Wang H. A fast multiphase image segmentation model for gray images. Comput Math Appl 2014;67:1559–81. https://doi.org/10.1016/J.CAMWA.2014.01.017.
[43] Yang Y, Wu B. Split Bregman method for minimization of improved active contour model combining local and global information dynamically. J Math Anal Appl 2012;389:351–66. https://doi.org/10.1016/J.JMAA.2011.11.073.
[44] Yang Y, Zhao Yi Wu B. Efficient active contour model for multiphase segmentation with application to brain MR images. Int J Pattern Recognit Artif Intell 2013;27:1355001https://doi.org/10.1142/S021800141355001X.
[45] Yang Y, Tian D, Jia W, Shu X, Wu B. Split Bregman method based level set formulations for segmentation and correction with application to MR images and color images. Magn Reson Imaging 2019;57:50–67. https://doi.org/10.1016/j.mri.2018.10.005.
[46] Meng X, Gu W, Chen Y, Zhang J. Brain MR image segmentation based on an improved active contour model. PLoS One 2017;12:e0183943https://doi.org/10.1371/journal.pone.0183943.
[47] Zheng Y, Gee JC. Estimation of image bias field with sparsity constraints. 2010 IEEE Comput. Soc. Conf. Comput. Vis. Pattern Recognit. IEEE 2010:255–62. https://doi.org/10.1109/CVPR.2010.5540205.
[48] Tustison NJ, Avants BB, Cook PA, Zheng Yuanjie, Egan A, Yushkevich PA, et al. N4ITK: improved N3 bias correction. IEEE Trans Med Imaging 2010;29:1310–20. https://doi.org/10.1109/TMI.2010.2046908.
[49] Shattuck DW, Sandor-Leahy SR, Schaper KA, Rottenberg DA, Leahy RM. Magnetic resonance image tissue classification using a partial volume model. Neuroimage 2001;13:856–76. https://doi.org/10.1006/NIMG.2000.0730.
[50] Sled JG, Zijdenbos AP, Evans AC. A nonparametric method for automatic correction of intensity nonuniformity in MRI data. IEEE Trans Med Imaging 1998;17:87–97. https://doi.org/10.1109/42.668698.
[51] Zhuge Y, Udupa JK, Liu J, Saha PK, Iwanage T. Scale-based method for correcting background intensity variation in acquired images. In: Sonka M, Fitzpatrick JM, editors. International society for optics and photonics vol. 4684. 2002. p. 1103. https://doi.org/10.1117/12.467067.
[52] Andersen AH, Zhang Z, Avison MJ, Gash DM. Automated segmentation of multispectral brain MR images. J Neurosci Methods 2002;122:13–23. https://doi.org/10.1016/S0165-0270(02)00273-X.
[53] Elad M, Aharon M. Image denoising via sparse and redundant representations over learned dictionaries. IEEE Trans Image Process 2006;15:3736–45. https://doi.org/10.1109/TIP.2006.881969.
[54] Dong W, Li X, Zhang L, Shi G. Sparsity-based image denoising via dictionary learning and structural clustering. CVPR 2011, IEEE 2011. p. 457–64. https://doi.org/10.1109/CVPR.2011.5995478.
[55] Shen Bin, Hu Wei, Zhang Y, Zhang Y-J. Image inpainting via sparse representation. 2009 IEEE Int. Conf. Acoust. speech signal process., IEEE 2009. p. 697–700. https://doi.org/10.1109/ICASSP.2009.4959679.
[56] Mairal J, Bach F, Ponce J, Sapiro G, Zisserman A. Non-local sparse models for image restoration. 2009 IEEE 12th Int. Conf. Comput. Vis IEEE; 2009. p. 2272–9. https://doi.org/10.1109/ICCV.2009.5459452.
[57] Elad M, Starck J-L, Querre P, Donoho DL. Simultaneous cartoon and texture image inpainting using morphological component analysis (MCA). Appl Comput Harmon Anal 2005;19:340–58. https://doi.org/10.1016/J.ACHA.2005.03.005.
[58] Xu Zongben, Sun Jian. Image inpainting by patch propagation using patch sparsity. IEEE Trans Image Process 2010;19:1153–65. https://doi.org/10.1109/TIP.2010.2042098.
[59] Ravishankar S, Bresler Y. MR image reconstruction from highly undersampled k-space data by dictionary learning. IEEE Trans Med Imaging 2011;30:1028–41. https://doi.org/10.1109/TMI.2010.2090538.
[60] Jorgensen JS, Sidky EY, Pan X. Quantifying admissible undersampling for sparsity-exploiting iterative image reconstruction in X-ray CT. IEEE Trans Med Imaging 2013;32:460–73. https://doi.org/10.1109/TMI.2012.2230185.
[61] Dong W, Shi G, Li X, Zhang L, Wu X. Image reconstruction with locally adaptive sparsity and nonlocal robust regularization. Signal Process Image Commun 2012;27:1109–22. https://doi.org/10.1016/J.IMAGE.2012.09.003.
[62] Pham DL, Prince JL. Adaptive fuzzy segmentation of magnetic resonance images. IEEE Trans Med Imaging 1999;18:737–52. https://doi.org/10.1109/42.802752.
[63] Chen X, Sang N, Huang R, Ren H. Estimation of image bias field by diffusion. Optik 2013;124:4590–3. https://doi.org/10.1016/J.IJLEO.2013.03.019.
[64] Rudin LI, Osher S, Fatemi E. Nonlinear total variation based noise removal algorithms. Physica D 1992;60:259–68. https://doi.org/10.1016/0167-2789(92)90242-F.
[65] Dobson DC, Santosa F. Recovery of blocky images from noisy and blurred data. SIAM J Appl Math 1996;56:1181–98. https://doi.org/10.1137/S003613999427560X.
[66] Huang Z, Huang L, Li Q, Zhang T, Sang N. Framelet regularization for uneven intensity correction of color images with illumination and reflectance estimation. Neurocomputing 2018;314:154–68. https://doi.org/10.1016/J.NEUCOM.2018.06.063.
[67] Borup L, Gribonval R, Nielsen M. Bi-framelet systems with few vanishing moments

characterize Besov spaces. Appl Comput Harmon Anal 2004;17:3–28. https://doi.org/10.1016/J.ACHA.2004.01.004.
[68] Ron A, Shen Z. Affine systems inL2(Rd): the analysis of the analysis operator. J Funct Anal 1997;148:408–47. https://doi.org/10.1006/JFAN.1996.3079.
[69] Cai J-F, Chan RH. A framelet-based image inpainting algorithm. Appl Comput Harmon Anal 2008;24:131–49. https://doi.org/10.1016/J.ACHA.2007.10.002.
[70] Cai JF, Ji H, Liu C, Shen Z. Framelet-based blind motion deblurring from a single image. IEEE Trans Image Process 2012;21:562–72. https://doi.org/10.1109/TIP.2011.2164413.
[71] Liu G, Lin Z, Robust Subspace Yu Y. Segmentation by low-rank representation. Proc. 27th Int. Conf. Mach. Learn 2010. p. 663–70. https://doi.org/10.1109/TCYB.2013.2286106.
[72] Boyd Stephen, Parikh Neal, C E, P B, E. J. Distributed optimization and statistical learning via the alternating direction method of multipliers. Found Trends Mach Learn 2011. https://doi.org/10.1561/2200000016.
[73] Cai J-F, Osher S, Shen Z. Split Bregman methods and frame based image restoration. Multiscale Model Simul 2010;8:337–69. https://doi.org/10.1137/090753504.
[74] Fang H, Yan L, Liu H, Chang Y. Blind Poissonian images deconvolution with framelet regularization. Opt Lett 2013;38:389. https://doi.org/10.1364/OL.38.000389.
[75] Chang Y, Fang H, Yan L, Liu H. Robust destriping method with unidirectional total variation and framelet regularization. Opt Express 2013;21:23307https://doi.org/10.1364/OE.21.023307.
[76] Cai J-F, Dong B, Osher S, Shen Z. Image restoration: total variation, wavelet frames, and beyond. J Am Math Soc 2012;25:1033–89. https://doi.org/10.1090/S0894-0347-2012-00740-1.
[77] Duan Y, Chang H, Huang W, Zhou J, Lu Z, Wu C. The L0 regularized Mumford-Shah Model for bias correction and segmentation of medical images. IEEE Trans Image Process 2015;24:3927–38. https://doi.org/10.1109/TIP.2015.2451957.
[78] Lin Z, Liu R, Su Z. Linearized alternating direction method with adaptive penalty for low-rank representation. 2011.
[79] Ahmed MN, Yamany SM, Mohamed N, Farag AA, Moriarty T. A modified fuzzy C-means algorithm for bias field estimation and segmentation of MRI data. IEEE Trans Med Imaging 2002;21:193–9. https://doi.org/10.1109/42.996338.
[80] Cocosco CA, Kollokian V, Kwan RK-S, Pike GB, Evans AC. BrainWeb: online interface to a 3D MRI simulated brain database. Neuroimage 1997;5:425.
[81] Ganzetti M, Wenderoth N, Mantini D. Intensity inhomogeneity correction of structural MR images: a data-driven approach to define input algorithm parameters. Front Neuroinform 2016;10:10https://doi.org/10.3389/fninf.2016.00010.
[82] Van Essen DC, Smith SM, Barch DM, Behrens TEJ, Yacoub E, Ugurbil K. The WU-Minn human connectome project: an overview. Neuroimage 2013;80:62–79. https://doi.org/10.1016/J.NEUROIMAGE.2013.05.041.
[83] WU-Minn HCP. 900 subjects data release: reference manual. 2015.
[84] Figueiredo MAT, Nowak RD. An EM algorithm for wavelet-based image restoration. IEEE Trans Image Process 2003;12:906–16. https://doi.org/10.1109/TIP.2003.814255.
[85] Mairal J, Elad M, Sapiro G. Sparse representation for color image restoration. IEEE Trans Image Process 2008;17:53–69. https://doi.org/10.1109/TIP.2007.911828.
[86] Dong W, Zhang L, Shi G, Li X. Nonlocally centralized sparse representation for image restoration. IEEE Trans Image Process 2013;22:1620–30. https://doi.org/10.1109/TIP.2012.2235847.